Mesoscale behavior of an aluminum-manganese dioxide-epoxy mixture under shock loading: from milli to nano-sized aluminum particles

Andrew Fraser
Marquette University

Recommended Citation
Fraser, Andrew, "Mesoscale behavior of an aluminum-manganese dioxide-epoxy mixture under shock loading: from milli to nano-sized aluminum particles" (2009). *Master's Theses (2009 -)*. Paper 7.
http://epublications.marquette.edu/theses_open/7

Mesoscale behavior of an aluminum-manganese dioxide-epoxy mixture under shock loading: from milli to nano-sized aluminum particles

By

Andrew W. Fraser, B.S.

Milwaukee, Wisconsin

December 2009

Abstract

The main focus of this thesis is to explore the dynamic shock compaction of multiple component mixtures, specifically Al-MnO_2-Epoxy. This will be facilitated by initially simulating the bulk dynamic response in a mesoscale configuration and then comparing these results to experimental data. The mesoscale simulations were performed in the shock code CTH. The first section will discuss the matching of experimental data to computational results. With the goal of determining the bulk shock Hugoniot, a one-dimensional flyer plate configuration was created while using a grain-geometry imported from an scanning electron microscope (SEM) micrograph of the mixture. Both the aluminum and manganese dioxide were assigned a strain dependent material strength: Aluminum- Johnson Cook and MnO_2- Johnson Ceramic II; this enabled the multiscale investigation down to the nanometer particle sizes as discussed in the second section.

The second section will discuss what effect changing the size of the aluminum particles and the alumina coating has on the formation of local hot spots. In addition the presence of voids and their effect on the hot spot formation was also investigated. A representative volume was created where aluminum particle diameters ranged from millimeter to nanometer; also, in the nano-sized setup, the alumina coating was varied from 0 to 3 nanometers. It was noticed that changing the aluminum grain size had a slight effect on the hot spot formation. Changing the alumina coating had an apparently random effect on the maximum temperature reached as no trend is clear. Also, it was found that inserting randomly placed voids into the epoxy binder created a large spike in initial temperature.

I. Acknowledgements

I would like to thank my family for their love and support throughout my time here at Marquette University.

Dr. Borg for always helping me whenever I had problems with my research and keeping me moving forward; and also thank you for bringing me along to various conferences where I was able to meet fellow researchers in the shock physics field. I would also like to thank Dr. Jon Koch and Dr. Otto Widera for being on my graduate committee.

Thank you to all my friends, especially my fellow “Dungeon” graduate students- Johnson, Abby, Scott, Morrissey, Dan and Jeff; we were all able to vent to each other when things weren’t going as planned with each of our projects… and we had some fun when we needed a break. I’ll miss our slacklining adventures and our Friday lunches…

I would like to thank the National Science Foundation Grant CTS-0521602 and the Navy NREIP Program for their sponsorship of my research. I would also like to thank the Naval Research Enterprise Intern Program and Gerrit Sutherland for giving me an opportunity to gain experience working in a government research lab.

II. Table of Contents

III. List of Tables

IV. List of Figures

1. Introduction

This work stems from experiments performed in Indian Head, MD at the Naval Surface Warfare Center (NSWC). The goal of an Air Force Research Labs study was to experimentally determine the bulk Hugoniot properties of an aluminum-manganese dioxide-epoxy (Al-MnO_2-Epoxy) mixture. The aim of this study is to compare the experimental results with corresponding one-dimensional shock compaction simulations using the two-dimensional shock physics code CTH [1]. These simulations utilize a high-resolution mesoscale approach in which each mixture constituent is individually resolved; thus the simulations capture the macroscale compaction behavior, including the transmission of stress and volumetric deformation, without the use of additional constitutive laws governing the small-scale compaction dynamics. In so doing, mesoscale simulations facilitate the exploration of material stress history and hot-spot formation. This approach has been successfully utilized to model a variety of energetic and inert heterogeneous materials [2,3,4].

In addition, the effects of grain size on the development of hot spots in mesoscale simulations are investigated. A two-dimensional representative volume was created to explore the effect when the aluminum grains are varied from a 30-micron diameter down to a 50-nanometer diameter. In addition, the aluminum oxide (Al_2O_3) coating around the aluminum particle was varied from 1 to 3 nanometers; this effectively changes the yield strength of the particle as the alumina has a higher yield strength compared to the aluminum alloy. In this setup, two MnO_2 particles compress the epoxy and aluminum particles much like the grain movement that was observed in the bulk computational setup used with the Air Force data.

2. Background

2.1. Introduction

The foundations of Shock Physics were originally developed in the 1800‘s by, among others, George Stokes, Pierre-Henri Hugoniot, and William Rankine [5]. Shock waves, characterized by compression wave fronts that propagate as a jump or discontinuous disturbance [6], have been intensively researched since the 1940’s. Shock Physics, the study of shock waves, has many modern applications such as spacecraft shielding, earthquakes, ordinances, and meteor impacts. The purpose of this review is to investigate the research that has been performed that relates to this thesis of mesoscale two-dimensional shock compaction of a heterogeneous mixture at multiple grain scales.

2.2. Experiments

Similar mixtures have been experimentally investigated by Millet et al. [7] and Ferranti, Jordan et al. [8]. In the study done by Ferranti et al., a light gas gun was used to determine the shock Hugoniot behavior of an Al-Fe_2O_3-epoxy composite. In these experiments a stoichiometric mixture of aluminum and iron-oxide powders combined with 60 and 78 vol.% epoxy were shock loaded with pressures up to 25 GPa. In the study, they found that the two mixtures and pure epoxy exhibited similar Us-Up Hugoniot behavior at speeds up to 450 m/s. But at about 550 m/s the 78 vol.% epoxy mixture exhibits a sharp transition towards pure epoxy behavior while the 60 vol.%

epoxy continues to deviate from the pure epoxy trend line; see Figure 1. It was proposed that the contrasting behaviors are due to various degrees of damage nucleating at solid inclusion sites in the epoxy. This is shown specifically in Figure 1where the 78 vol.% epoxy mixture's Us-Up curve approaching and then falling under the pure epoxy trend line at higher Up values.

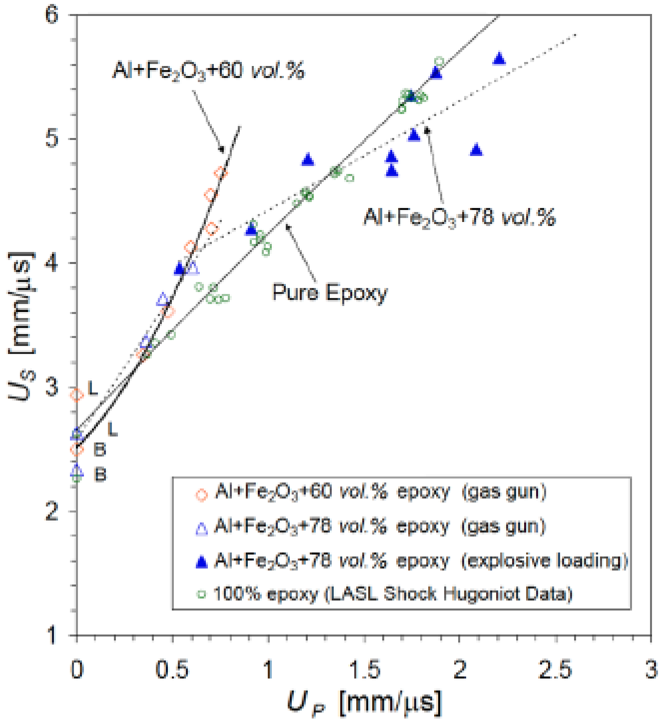

Figure 1: Comparison of Us-Up Hugoniot data for the aluminum, iron oxide, epoxy mixture along with pure epoxy

2.3. *Simulations*

Research has been performed using various types of hydrocodes; they may be Lagrangian, Eulerian, or arbitrary Lagrangian Eulerian (ALE). All use a mesh that tile the domain. The difference is if the mesh deforms and moves with the grains (Lagrangian) or is stationary throughout the calculation (Eulerian). The Lagrangian methods are less computationally extensive, but are limited to the amount of deformation the calculation can accept before errors occur. The ALE method generally runs in a nearly Lagrangian manner while the mesh is locally adjusted so that larger deformations can be resolved. It should also be noted that the term “hydrocode” is a misnomer used by many today to describe codes that solve shock waves. This term was originally used to describe shock wave solving codes in the 1950’s that neglected deviatoric stress (an assumption normally for fluids) in order to reduce the cost of early computations; however, the term stuck with the computer codes even though the deviatoric stress was included in codes in the 1960’s. [9]

In work done by Eakins et al. [10] they explain that the shock compression process of granular material is different from full density, homogenous materials. This process can result in unique physical interactions caused by the void collapse not seen in homogeneous materials. It is difficult to see these effects through experiments though, because they occur on micro-level time and length scales that probes (stress gages, VISAR) cannot measure; instead these probes provide a response that is averaged over a specified area. Therefore, to investigate these effects, modeling at the particle must be used via computer simulations. This can lead to a better understanding of the microscopic level phenomena that lead to the experimentally observed macroscopic phenomena.

Eakins [10] goes on to explain that many modern simulations today utilize oversimplified, computer-generated microstructures such as spheres or cubes. Ideally, one would use real micrographs as the configuration in the simulation. This is the process which Eakins [10] has developed. In this process, they import a micrograph into a hydrocode. To do this they (1) manually threshold each grain and separate each phase into binary images; (2) vectorize each binary image of each phase; (3) convert the vectorized image into particle descriptions that are directly inserted in the CTH setup file. A comparison of the SEM micrographs and CTH generated image can be seen in Figure 2.

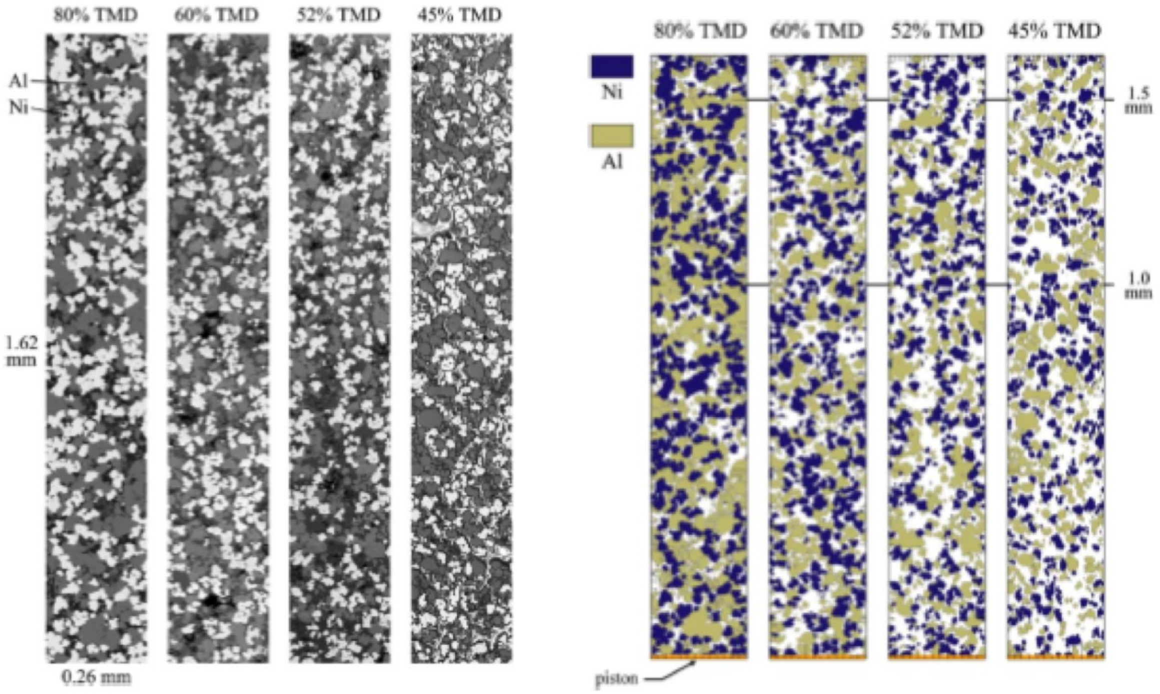

Figure 2: Comparison of SEM micrographs and CTH generated material plot after importation process into setup file

The results obtained by Eakins with a binary Ni and Al mixture compare well with experimentally obtained results as shown in the Us-Up graph shown below in Figure 3.

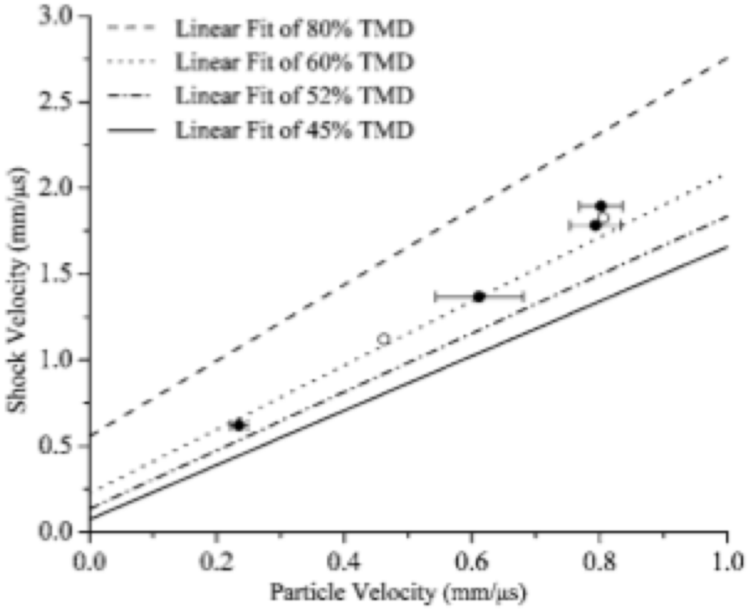

Figure 3: Comparison of experimental data (data points) and computational data (lines)

Another benefit found by Eakins in using experimentally acquired images is the potential to model the actual deformation of particles which are otherwise unable to be observed in experiments or simulated microstructures due to the lack of heterogeneities. In the work by Eakins, they were able to observe the focused flow (or jetting), particulation, and vortex formation; these are the mechanical phenomena that contribute to the local plastic deformation, energy dissipation, and propagation of the compressed region. Figure 4 shows an example of focused flow in Eakins work. One can see the flow of the aluminum particle (marked “A”) through nickel barriers. This flow can result in increased velocity and high localized temperature and pressure. It is because the geometry was created from the SEM micrograph the focused flow was able to be observed; in a representative volume it would be difficult to accurately observe this type of mechanical behavior.

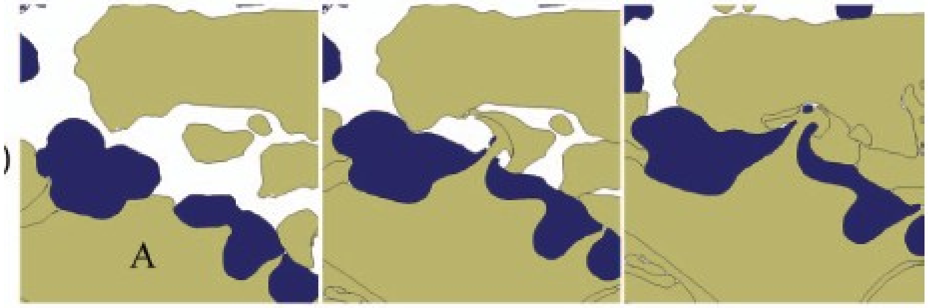

Figure 4: Example of singular focused flow of aluminum (gold) through nickel barriers (blue) [10]

Using an importation method like Eakins' for creating the computational geometry can also be faster than trying to create a representative volume. It can take many hours trying a representative geometry that matches the measured volume fractions of the constituents and best models the actual shapes of the particles.

Similar work has been reported by Benson and Conley [4]. They created a similar process that would import SEM geometry into a finite element analysis. In their simulations, they considered the effect of heat conduction and viscosity on the formation of hot spots, small regions of high temperature where reaction may initiate. They found that at the grain scale they were investigating, particles from 1 to 15 micrometers, conduction had no significance during the formation of hot spots within the shock front; conduction was not rapid enough to dissipate the heat in the particles. The results were the same when conduction was included and when it was not included (adiabatic). With regards to the viscosity, they found that viscosity not only spreads out the shock front, but also reduces the temperature extremes and suppresses particle jetting.

In similar studies done by Baer et al. [3 ,11, 12], a plastic bonded explosive, PBX 9501, was isentropically loaded using the Z facility at the Sandia National Laboratories. The explosive consisted of 95% HMX, 2.5% polymer binder, and 2.5% nitroplasticizer; in the mixture, the HMX forms the skeletal structure with large and small grains dispersed throughout the sample while the binder and plasticizer are in the interstitial regions between the grains. He, like Eakins [10], points out the effect that heterogeneity can have on shock propagation and energy release in the shock wave- i.e. hot spots. For example, to trigger a reaction in a monolithic crystal of high explosives, a pressure of 10 GPa is required; however for the same material in a porous state, initiation can occur in pressures less than 1 GPa. Unlike the research performed by Eakins [10] where he imported the SEM micrograph into the simulation, Baer [3, 11, 12] instead only created a representative volume of the PBX material. Figure 5 shows the SEM image of the PBX and Figure 6 shows the 3-D representative volume created. Notice how the HMX crystals in Figure 6 are triangles and quadrilaterals while the crystals in Figure 5 are more complex.

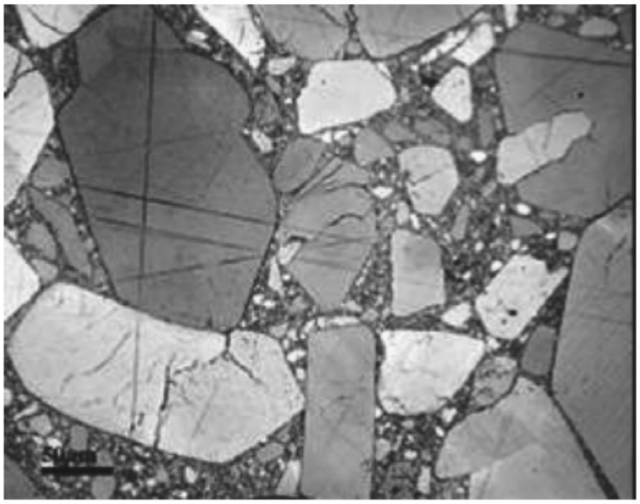

Figure 5: SEM image of PBX 9501

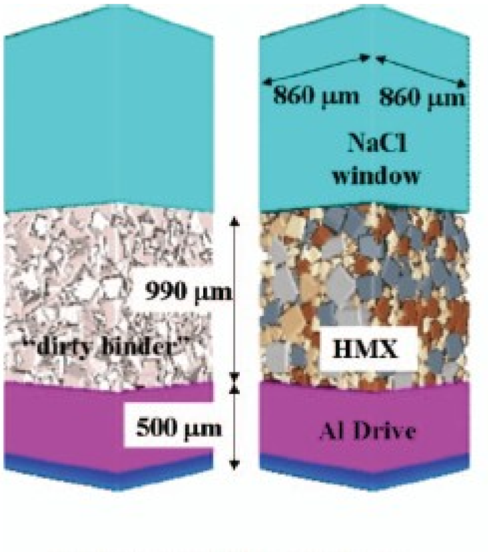

Figure 6: Three dimensional representative volume of Figure 5

3. Experiments

The goal of the experimental effort was to determine the bulk Hugoniot of a mixture containing 31.08% MnO_2, 23.77% Al and 45.15% Epon 826 (epoxy) by volume. Experimental data was obtained using a variety of instrumentation including Velocity Interferometer System for Any Reflector (VISAR), PVDF gages, and manganin gages [13]. Although experiments were carried out at Los Alamos National Labs (LANL) and the Naval Surface Warfare Center at Indian Head, MD (NSWC-IH), the NSWC configuration was chosen as the baseline for the simulations. Induced particle velocities ranged from 180 m/s to 2,770 m/s over all the experiments. Table 1 summarizes the shock states achieved for all of the data, both LANL and NSWC-IH.

[1]**Table 1:** Shock states achieved during experiments

Exp. No.	**Us (km/s)**	**U_s – Tilt Corrected (km/s)**	**Up (km/s)**	**P (GPa)**
JJH14	4.16 ± 0.60	4.28 ± 0.50	0.94 ± 0.34	10.5 ± 3.9
JJH15	5.30 ± 0.38	5.36 ± 0.31	1.36 ± 0.25	18.9 ± 3.7
JJH16	4.85 ± 0.22	4.90 ± 0.08	1.42 ± 0.39	18.1 ± 4.9
JJH28	2.90 ± 0.15		0.18 ± 0.03	1.4 ± 0.2
JJH28 PVDF	2.85		0.17	1.3 ± 0.1
JJH29	3.61 ± 0.32		0.35 ± 0.07	3.3 ± 0.1
JJH30	3.30 ± 0.07		0.63 ± 0.02	*5.4 ± 0.2*
JJH54	4.84 ± 0.34	4.91 ± 0.27	1.38 ± 0.06	17.6 ± 1.2
JJH55	5.02 ± 0.44	5.09 ± 0.32	1.36 ± 0.06	18.0 ± 1.4
JJH56	4.07 ± 0.24	4.16 ± 0.11	0.81 ± 0.03	8.8 ± 0.4
JJH57	4.24 ± 0.26	4.30 ± 0.18	0.81 ± 0.03	9.0 ± 0.5
JJH58	5.37 ± 0.18	5.38 ± 0.16	1.76 ± 0.09	24.5 ± 1.4
JJH59	5.08 ± 0.24	5.15 ± 0.12	1.78 ± 0.09	23.9 ± 1.3
JJH60	4.80 ± 0.22	4.86 ± 0.10	1.29 ± 0.19	16.2 ± 2.4
JJH61	4.78 ± 0.25	4.86 ± 0.13	1.12 ± 0.19	14.2 ± 2.4
JJH62	4.45 ± 0.31	4.46 ± 0.29	1.33 ± 0.12	15.4 ± 1.7
JJH63	4.16 ± 0.32	4.20 ± 0.28	1.36 ± 0.12	14.8 ± 1.6
JJH64	3.96 ± 0.26	3.99 ± 0.22	0.90 ± 0.13	9.3 ± 1.4
JJH65	3.98 ± 0.37	4.00 ± 0.36	0.91 ± 0.13	9.3 ± 1.6
JJH31	3.12 ± 0.22		0.57 ± 0.04	4.6 ± 0.4
JJH32	2.98 ± 0.15		0.41 ± 0.03	3.2 ± 0.3
2S-318	5.578		1.365	19.87
2S-333	4.978		2.269	11.95
2S-336	5.333		2.770	16.31
JJH120	3.64 ± 0.13		0.32 ± 0.06	3.0 ± 0.6
JJH121 – man.	3.88		0.48	4.8 ± 0.1 (I) 3.4 ± 0.7 (T)
JJH121 PVDF	3.88		0.41	4.2 ± 0.2 (I)
JJH122 – man.	3.93		0.48	4.9 ± 0.2 (I) 4.1 ± 1.8 (T)

The experiments performed at the NSWC- Indian Head were performed on their four-inch one stage light gas gun. Images of the facility and the sabots used are presented in Figure 7.

---

[1] Distribution A: Approved for public release 96 ABW/PA 09-03-08-385

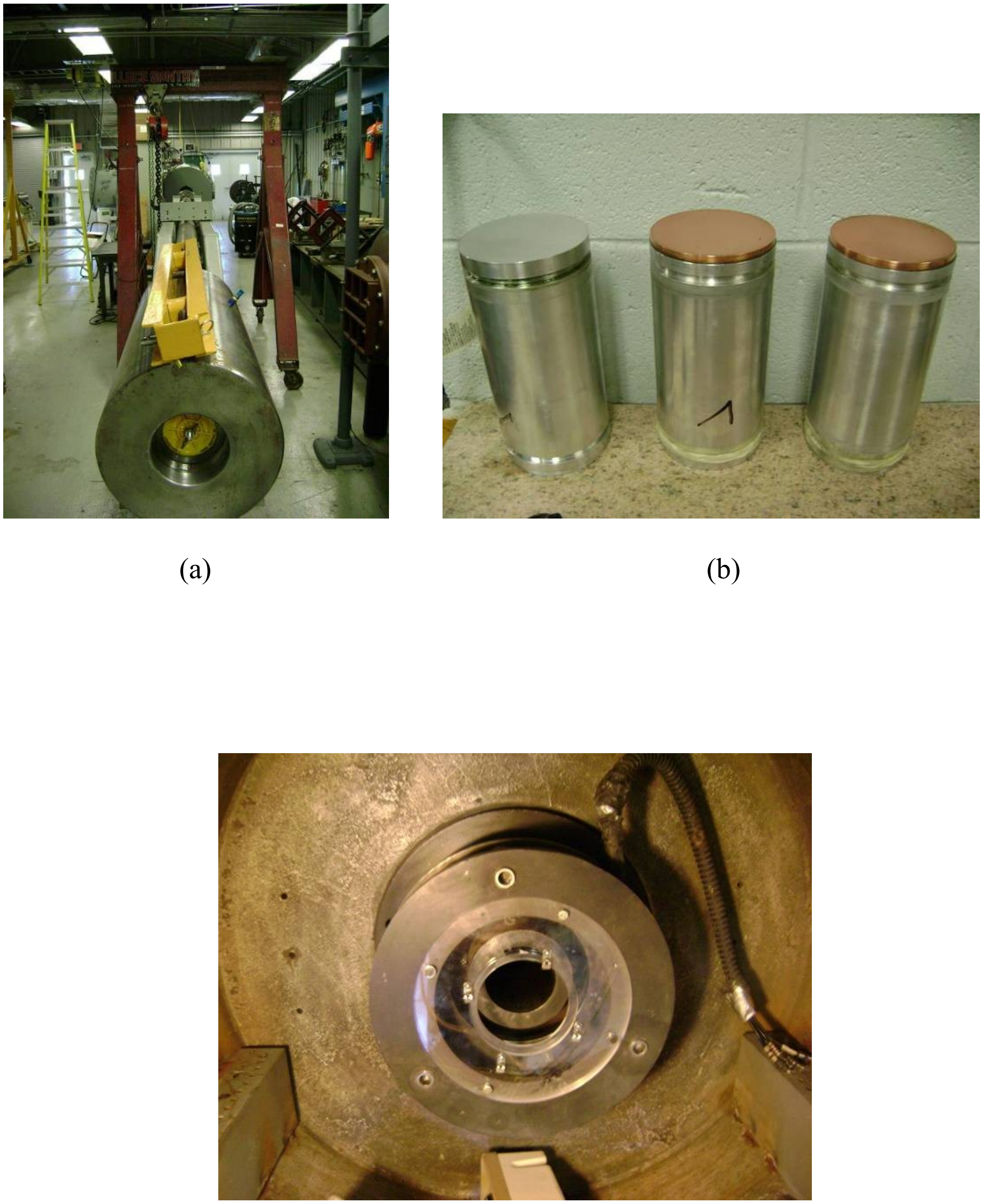

(a) (b)

(c)

Figure 7: (a) NSWC-Indian Head Gun Facility: The four inch gun. (b) Sabots used for gas gun shots. (c) Target holder

The samples of the Al-MnO_2-Epoxy mixture were prepared at the Air Force Research Labs (AFRL) in Eglin, FL. The NSWC experiments were carried out in a flyer plate configuration; see Figure 8 for a schematic. The target was such that each shot impacted three 31.75 mm diameter and 3.18 mm thick samples in a laterally unconfined configuration. PVDF or manganin gages were epoxied in front and behind each sample with a second sample epoxied after the rear gage. Aluminum or copper flyer plates, which were 3.75 mm thick, were used to impact the 6.35 mm aluminum or copper cover plates. The induced particle velocities in this test configuration were 320, 410, and 480 m/s.

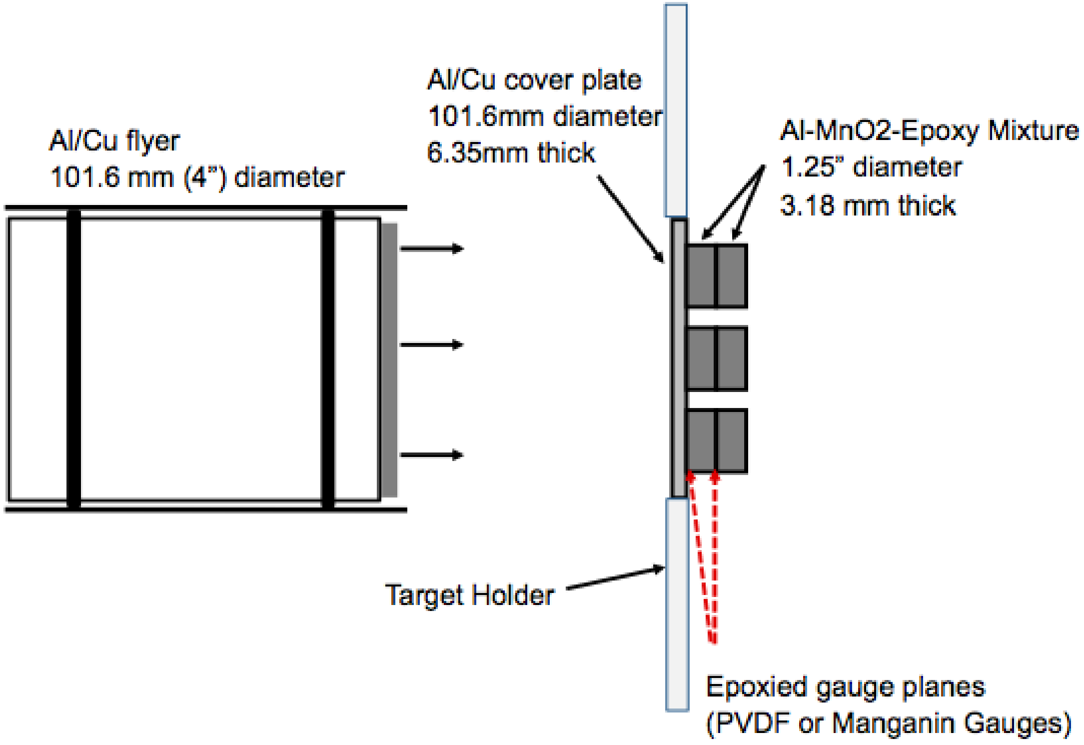

Figure 8: Experimental setup for baseline target configuration at NSWC- Indian Head.

4. Computer Simulations

4.1. *Geometry*

In order to perform computational simulations of the shock compaction process, a setup geometry was needed. A Scanning Electron Microscope image seen below in Figure 9 was used to create this geometry.

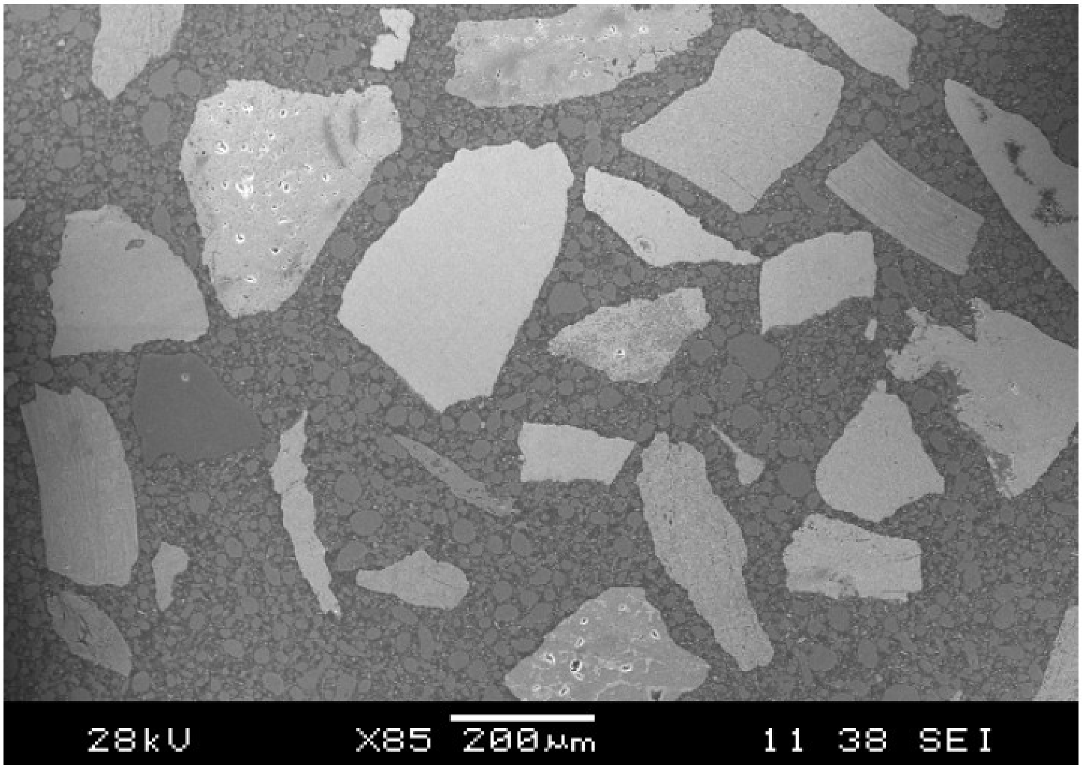

Figure 9: SEM image of Al-MnO_2-Epoxy mixture.

A process which converted the digital image to CTH input coordinates was developed by Eakins and Thadhani at the Georgia Institute of Technology [10]. This process starts with thresholding the image to make all the particles white and all the epoxy black. To do this, the open source program *GNU Image Manipulation Program (GIMP)* [14] was used to edit Figure 9; the program was used to select the boundary of each grain in order to edit its color. Since, in this case, there are three materials- epoxy, manganese dioxide, and aluminum, two edited images needed to be created; one where the aluminum particles were thresholded, and one where the manganese dioxide particles were thresholded. Due to the low contrast between the particles and epoxy, the particles were visually thresholded by selecting the particles using the "fuzzy select tool"(threshold= 15.0) or "free select tool" and then making them to be white in order to accentuate the particle boundaries; Figure 10 presents the two edited images respectively.

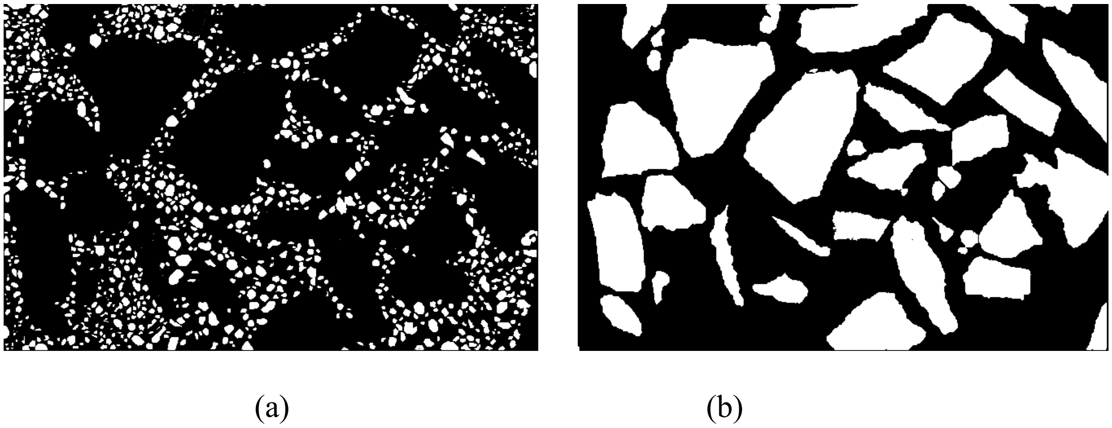
(a) (b)

Figure 10: Edited images of the physical domain presented in Figure 3. (a.) aluminum is white while epoxy and manganese dioxide are black; (b.) manganese dioxide is white while epoxy and aluminum are black

Once these images were created, they were imported in the software program, *AlgoLab Raster to Vector Conversion Toolkit* [15]. This program detects the grain boundaries in each image and creates outlines of each grain. The outlines of each image were then saved as vector files; this allows for the vector description of the grains to be properly scaled. In so doing the final coordinates will correspond with the SEM image scale. Once the files are saved, it is then imported into *AutoCAD* [16]; this is done to convert the vector .dxf files to an .R12 format that is compatible with a *MATLAB* [17] code developed by Georgia Tech. This code converts the .R12 file into CTH coordinates that can be directly inserted in the CTH setup file.

In order to reproduce the full experimental geometry in CTH, a larger domain was required than was provided by the SEM image. This was accomplished by mirroring the original image twice in the longitudinal direction. Due to the resolution of the SEM images as well as the post processing, not all of the aluminum particles are resolved via our image conversion process. Therefore, in order to match the volume fraction of the computational work with the experimentally measure volume fraction, aluminum spheres were randomly inserted into the domain; MnO_2 particles were also removed for the same reason.

Once this was done, the bulk density within CTH (2.70 g/cc) still did not match the density measured in the experiments (2.59-2.61 g/cc). Upon closer inspection of the SEM images, it was noticed that the MnO_2 particles were not fully consolidated but rather porous. The density of the MnO_2 in CTH was then lowered from 5.026 g/cc to 4.55 g/cc in order to match the bulk densities and account for the porous nature of the MnO_2. The resulting computational domain from CTH is shown below in Figure 11c while the corresponding views of the SEM image and the computation geometry can be seen in Figure 11a and Figure 11b.

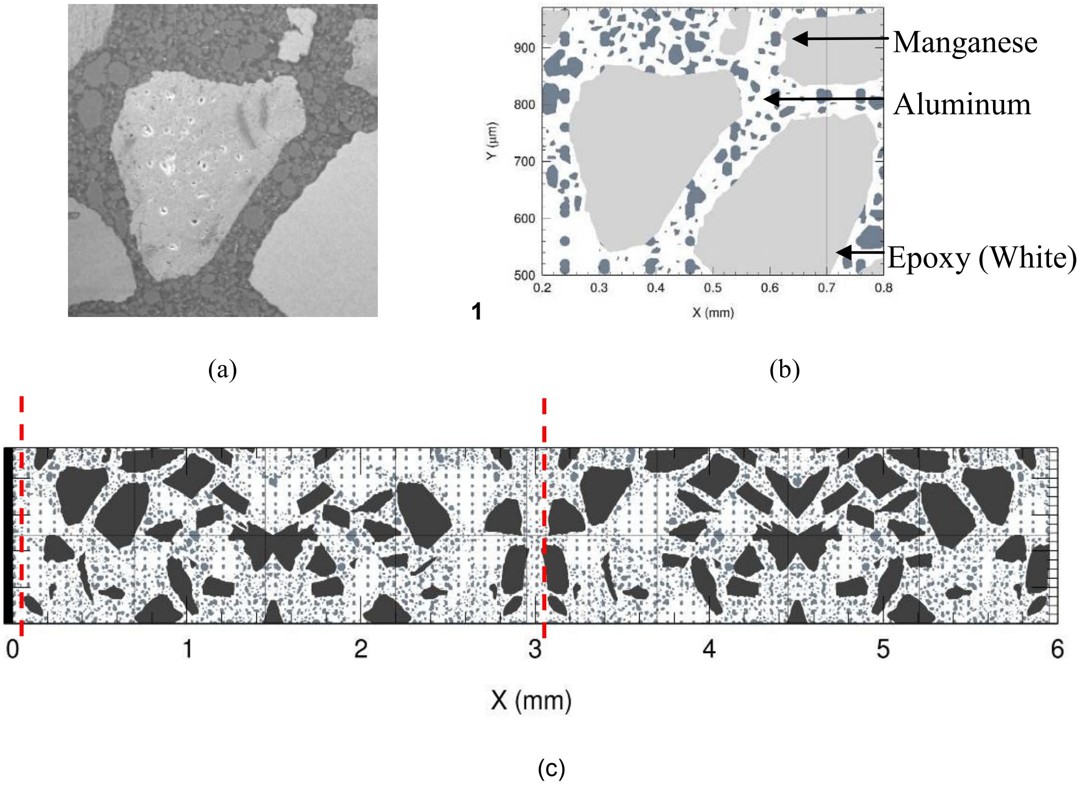

(a)

(b)

(c)

Figure 11: Computational domain. (a) Enlarged view of SEM image. (b) Geometry corresponding to (a) that was imported into CTH. (c) Entire computational geometry utilized in mesoscale simulations. Dashed lines correspond to gage locations in physical experiment

4.2. Numeric setup

The aluminum driver plate, which can be seen on the far left of Figure 11c, travels from left to right at a specified particle velocity. The driver plate in the simulations was represented as a rigid body where it has no stress propagating through the material. This reduces computing requirements for the overall domain without sacrificing accuracy in the overall simulation. Periodic boundary conditions were used at the upper (y=1 mm plane) and lower (y=0 mm plane) surfaces. The rear of the sample (i.e. the right domain) had a free surface boundary condition where the pressure in ghost cells is zero and mass is allowed to flow out of the domain. The computational resolution was such that there was a minimum of eleven cells across the smallest grain; this equals 3300 nodes in the x-direction (0.6005 cm), 550 nodes in the y-direction (0.1 cm) and 1.82 μm/cell.

4.3. Material Properties

The following describes the constitutive models for each material utilized in these calculations; Table 2 summarizes their respective material properties. It is important to keep in mind that the mesoscale configuration means each constituent is modeled as a fully consolidated material. No mixtures models are necessary because the simulation is resolving each grain.

4.3.1. Aluminum

Each material was assigned an appropriate built in equation of state and strength model. One of the great advantages of mesoscale simulations, over bulk simulations, is that mixture models are not necessary to describe the bulk material behaviors. The bulk behavior is resolved by integrating the over the entire domain, which consists of a collection of grains. The simulation, which resolves each material separately, assigns the bulk material properties to each individual grain. Aluminum was assigned a Johnson-Cook strength model and a Mie-Gruneisen equation of state. The Johnson-Cook strength model is given by the equation

$$\sigma \quad \varepsilon \quad \dot{\varepsilon}$$

Equation 1

where ε_p is the equivalent plastic strain, $\dot{¿}$ is the plastic strain-rate, and A, B, C, n, and m are material constants. While the normalized plastic strain-rate and temperature in Equation 1 are defined as

$$\dot{¿} \qquad \frac{\dot{}}{\dot{¿}} \tag*{Equation 2}$$

$$T^{*} := \frac{T}{T_m -} \; - \tag*{Equation 3}$$

where $\dot{¿}$ is a plastic strain-rate defined by the user, T_0 is a reference temperature, and T_m is a reference melt temperature. The Johnson-Cook strength model was chosen because it captures strain-rate dependent behavior; it is known that materials can work harden while under strain [18]. This is needed for the multiscale work described in Section 5. The Johnson-Cook has been previously implemented within CTH and has numerous materials built into the model, including aluminum.

The Mie-Gruneisen equation of state is based on the Mie-Gruneisen approximation given by $\Gamma = \quad \partial \quad \partial \quad _{\rho}$ where Γ is the Gruneisen parameter and is only a function of density [19]. This leads to a linear relationship between pressure and density given by

$$P \;\; \rho \qquad = \qquad + \Gamma \;\; \lfloor \qquad\qquad \rfloor \tag*{Equation 4}$$

where P_R and E_R are a reference pressure and energy generally given by the Hugoniot. To find temperature, it is assumed that the constant-volume specific heat $C_v = \partial \quad \partial$ is constant which leads to

$$E \;\; \rho \qquad = \qquad + \;\; \lfloor \qquad\qquad \rfloor . \tag*{Equation 5}$$

4.3.2. *Manganese Dioxide*

The manganese dioxide was assigned a Johnson-Holmquist II (JH-2) ceramic model [20]; as implemented in CTH, this functions both as an equation of state and a strength model. The reason the JH-2 model was selected for this study is because it models the strain softening behavior that ceramics exhibit in experiments. The JH-2 model computes the yield surface depending on a scalar damage parameter. Figure 12 presents strength curves for a ceramic material in the JH-2 model. One can see that initially the material has a specific strength curve; but as the damage accumulates, the strength curve is reduced.

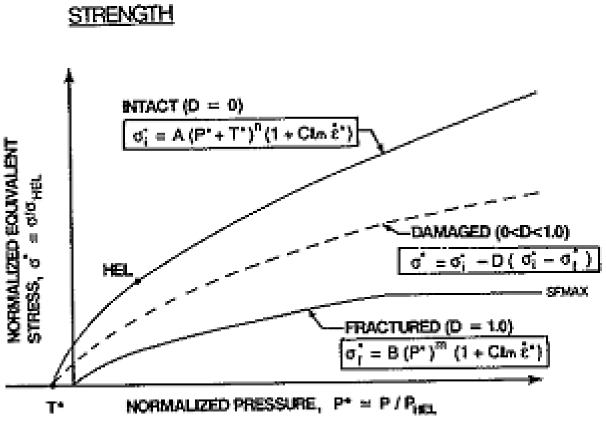

Figure 12: Strength in the JH-2 model [20].

In order to capture this behavior a damage parameter, D, is introduced. This parameter is bound between zero and one (0≤D≤1) and is used to calculate the normalized flow stress as follows:

$$\sigma = \quad - \quad - \tag*{\textbf{Equation 6}}$$

where σ and σ are the intact and fractured normalized flow stresses respectively. The normalized flow stresses $\sigma \ \sigma \ \sigma$ are found from the general form $\sigma =$ where σ is the plastic flow stress and σ_{HEL} is the Hugoniot Elastic Limit (HEL). The normalized intact and fractured stress are found from

$$\sigma = \qquad + \qquad + \qquad . \qquad \textbf{Equation 7}$$

$$\sigma = \qquad + \qquad . \qquad \textbf{Equation 8}$$

The material constants in these equations are *A*, *B*, *C*, *M*, *N*, and SFMAX; note that SFMAX is a parameter that can limit the fracture strength by $\sigma \leq$ in order to provide flexibility in defining the fracture strength. The normalized pressure P^* is found from $P^* =$ where P is the pressure and P_{HEL} is the pressure at the HEL. The normalized maximum tensile hydrostatic pressure is found from $T^* =$, where *T* is the maximum tensile hydrostatic pressure the material can withstand.

The damage parameter is expressed as

$$D = \sum \frac{}{\varepsilon} \qquad \textbf{Equation 9}$$

where Δ is the plastic strain during a cycle of integration and ε is the plastic strain to fracture under a constant pressure, P; the expression for this is

$$\varepsilon = \qquad + \qquad \textbf{Equation 10}$$

where D_1 and D_2 are constants and P^* and T^* are as defined previously.

4.3.3. Epoxy

The epoxy was assigned an elastic-perfectly plastic strength model where Hooke's law governs the elastic regime:

$$\sigma = \qquad \textbf{Equation 11}$$

where ε and E are the strain and Young's Modulus, respectively. A von Mises yield condition with a constant plastic flow stress prescribed by the user governs the elastic to plastic transition.

For the equation of state, the epoxy was given the Mie-Gruneisen model in conjunction with a History Variable Reactive Burn (HVRB) Model in order to computationally facilitate a phase transformation. It is known that epoxy undergoes a phase transformation at 23.1 GPa [21]. In this transition the chains of the epoxy are pushed together to the point that inter-chain interactions are possible where covalent bonds break in the epoxy chains (see Figure 13) and tetravalent bonds among the chains are formed.

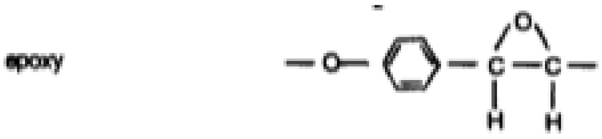

Figure 13: Idealized monomer structure of epoxy [21]

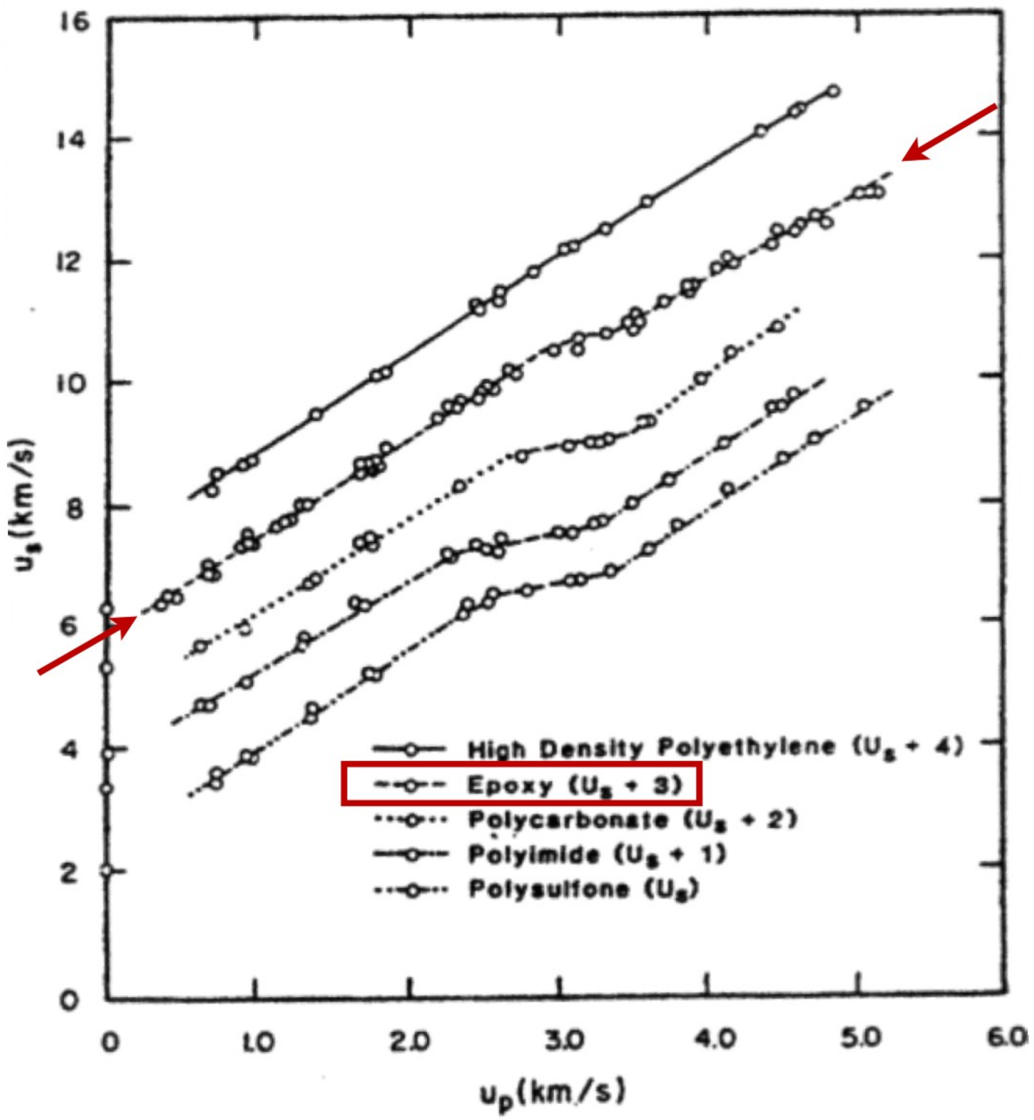

Figure 14: Shock speed vs. particle speed graph of the epoxy transition [21]

The result is a slight shift in the reference Hugoniot of the epoxy. The particle velocity (Up) versus shock velocity (Us) is presented in Figure 11 and the epoxy has been indicated with an arrow for clarity. The phase transition can be easily identified as an intersection of two linear Us-up Hugoniots at a particle velocity near 3.5 km/s.

The HVRB model was used as a trigger in the hydro-code to initiate the phase transition. The HVRB model is a pressure-dependent continuum reaction model in which extent of reaction, λ, is integrated over time at a given mass point. The model has the following form:

$$\lambda = -\left(\quad \right)^{X} \qquad \textbf{Equation 12}$$

$$\phi = \frac{1}{\tau} \int^{P} \qquad \textbf{Equation 13}$$

where X, P_R and z are reaction rate parameters, and P_i is the threshold pressure for reaction. Although the HVRB model is typically used to describe reaction rates for explosives, where solid reactants equation of state is mixed with gaseous products equation of state, in this case it was used to transition from a solid (phase I) to a solid (phase II) equation of state. Thus default reaction parameters were mostly used to simplify the transition. The parameters P_R and z determine the pressure dependence of time and distance to reaction and are usually fit to wedge test data. The exponent M controls the time delay to pressure build up behind the shock front and X determines the rate at which the reaction proceeds to completion; τ_0 is used to make ϕ dimensionless and is not an independent constant. Table 3 lists the input HVRB parameters used in this study. The use of an HVRB model allowed for the use of two Mie-Gruneisen equations of state for the epoxy; one for phase I when the local pressure in the epoxy is below the 23.1 GPa reaction threshold, and one for the transition phase when the local pressure is above the threshold. A second set of simulations were performed in which the epoxy was assigned a Mie-Gruneisen equation of state which corresponded to pure phase II epoxy;

this was done in order to establish the full transition compaction behavior. This is of especial interest in a mesoscale configuration where the localized stresses can vary thus either aiding or delaying a pressure driven phase transition mechanism. The parameter constants associated with each phase of the epoxy is listed in Table 2.

Table 2: Equation of State and Constitutive Material Parameters

Parameter	**MnO2**† [22,23,24]	**Al** [25,26]	**Epoxy**†† Phase I [22,27, 28]	**Epoxy** Transition Phase [22,27,28]	**Epoxy** Phase II [22,27,28]
Density, ρ [*g/cm3*]	4.55	2.703	1.19	1.19	1.19
Zero stress shock speed, C_0 [*km/s*]	3.632	5.288	2.67	7.88	2.88
Hugoniot slope, s	1.52	1.3756	1.55	0.01	1.35
Grüneisen coefficient, G=$V(\partial P/\partial E)_V$	1.25	2.14	2.18	2.18	2.18
Specific heat, C_V [*J/(g-K)*]	0.67	0.885	2.1	2.1	2.1
Bulk Dynamic yield strength, Y [*GPa*]	7.5	0.29	0.069	0.069	0.069
Poisson's ratio, ν	0.28	0.32	0.36	0.36	0.36
Bulk Modulus, K [*GPa*]	34.4	75.5	8.48	73.9	9.87
Fracture strength, σ_s [*GPa*]	N/A	60	60	60	60

† Johnson-Holmquist II Strength [20] †† Epon 828 Data

Table 3: History Variable Reactive Burn (HVRB) Parameters

Parameter	**Value**	**Parameter**	**Value**
Reaction rate, X [*unit less*]	1.0†	Time delay, *M* [*unit less*]	1.5†
Pressure threshold, P_i [*GPa*]	23.1	Reaction rate, P_R [*GPa*]	5.0†
Pressure dependence, z [*unit less*]	3.0†		

† Default [29]

4.4. Results

4.4.1. Material Movement

Material plots were generated in order to explore the grain-on-grain and grain-binder interactions within the mixture matrix. Figure 15 presents the two-dimensional stress response of the material where the contours represent pressure. The contours demonstrate that the epoxy undergoes larger deformation than does the more rigid MnO_2 or Al; thus the load is carried by the epoxy. The result is a spatially and temporally varying stress state behind the initial compaction wave. The post processor indicates stresses below the legend as white and clips all the stresses above the legend as black. Thus, in Figure 15, a spatially large low-pressure precursor stress can be seen as the all-white portion located ahead of the shock front. For these relatively small grains the shock compaction of the entire computational domain takes less than 2 μs.

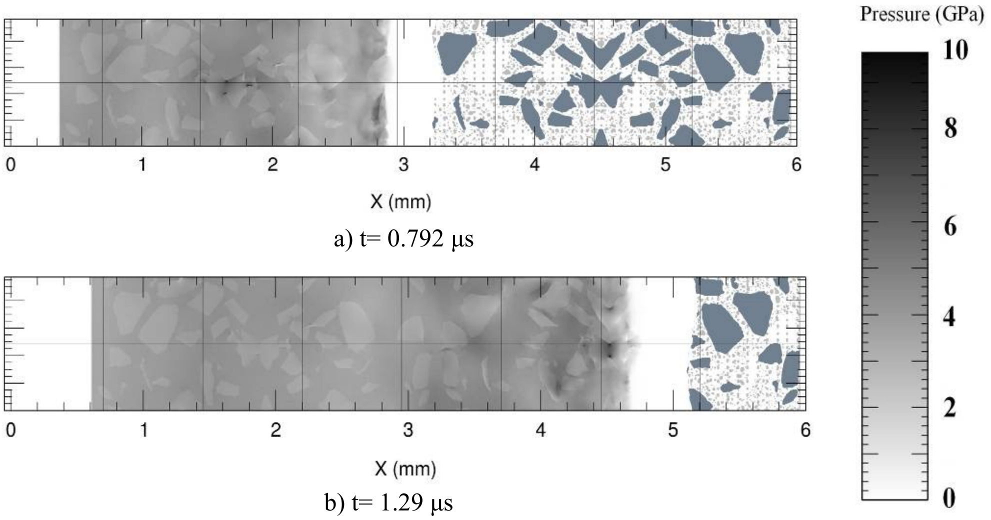

a) t= 0.792 μs

b) t= 1.29 μs

Figure 15: Compaction response of the Al-MnO_2-Epoxy mixture at a flyer plate velocity of Up= 480 m/s.

4.4.2. Conduction

One area of interest is the conduction of heat through each grain. Will there be significant heat conduction through any grain when dealing with the micron timescale? What is the characteristic length associated with the adiabatic assumption when applied to a heterogeneous material? Simple calculations were made in order to roughly estimate the thermal diffusion distance. As suggested by Meyers [19], the characteristic dimensions of heat diffusion distance can be estimated by

$$d = \quad , \qquad \textbf{Equation 14}$$

where d is the distance heat is conducted, α is the thermal diffusivity, and t is the time under strain; for aluminum, α is about 0.65cm^2/s from 300 K to 700 K [30]. The time under strain is estimated by dividing the grain radius by the shock speed. To see what the largest depth of conduction possible, the smallest shock speed of 2.9 km/s was used ($t = \frac{10x10^{-}\ m}{2.9x10\ m/s}$) to get a time of 3.448 ps. The resulting distance of conduction is $d =$ around a 20 μm diameter aluminum particle. Thus the diffusion diameter is 10 times smaller than the grain diameter. As a result it was concluded that the adiabatic assumption is still valid for this mixture. However, this does not account for possible heat transfer from the epoxy to the aluminum particle and including a conduction model in the simulations will be considered in future work.

4.4.3. Bulk Response

The bulk Hugoniot response was obtained by locating the bulk compaction wave front at various snapshots in time during the simulation. For each snapshot, the longitudinal stress was averaged in the lateral direction in order to produce a single instantaneous bulk wave profile as it traversed the domain. The compaction wave location was assigned to the half-height of the transmitted longitudinal stress wave front. By knowing the location of the bulk compaction wave and the time at which the snapshot was obtained, the compaction wave speed could be calculated. Figure 16 presents the averaged bulk compaction wave speed through the sample, as a function of longitudinal position. Each trace represents a different flyer plate particle velocity. Figure 16 indicates that the bulk compaction wave speed is fairly constant as it traverses the sample. From these results it appears that the wave speed reaches steady state at approximately 3 mm, which corresponds to roughly 12 MnO_2 grain characteristic lengths. From this data the compaction-particle velocity relationship can be obtained and projected onto density-stress space via the Rankine-Hugoniot relations.

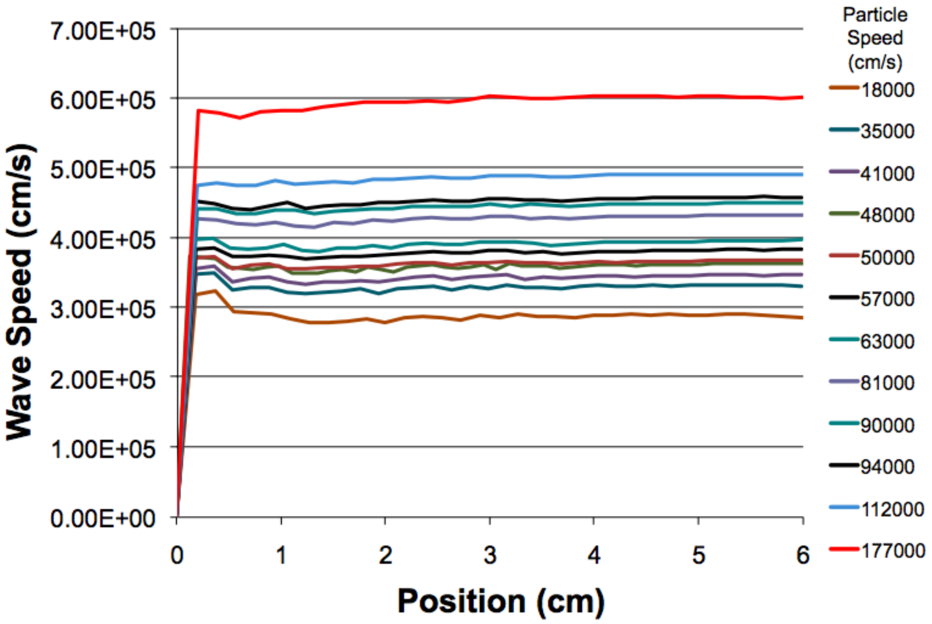

Figure 16: Comparison of the averaged wave speeds at various positions in the sample.

Figure 17 presents a comparison of the experimental and simulated bulk compaction response. The experimental results were fit to a linear Us-Up Hugoniot and projected onto density-stress space via the Rankine-Hugoniot equations

$$P = \quad .$$ **Equation 15**

$$\frac{1}{\rho} = \frac{1}{\rho}\left(\qquad \right)$$ **Equation 16**

The Us-Up experimental data clearly indicates a change in slope near particle velocities of 0.80 km/s. As discussed in Section 4.3.3, it is well documented that epoxy undergoes a phase transition at these conditions [21]. Thus the discontinuity in the Us-Up data is associated with the epoxy phase transition. At low stress levels, the experimental data and simulated response agree very well, while at high stress levels near 25 GPa, the computational data splits the two experimental points. One must assume that by the time the mixture reaches these pressures, nearly all epoxy should be in the third phase. However, in the transition region, the experimental data exhibits substantial scatter, which may be due to variations in the mixture. The sensitivity of the transition region is unknown and could be explored in future work.

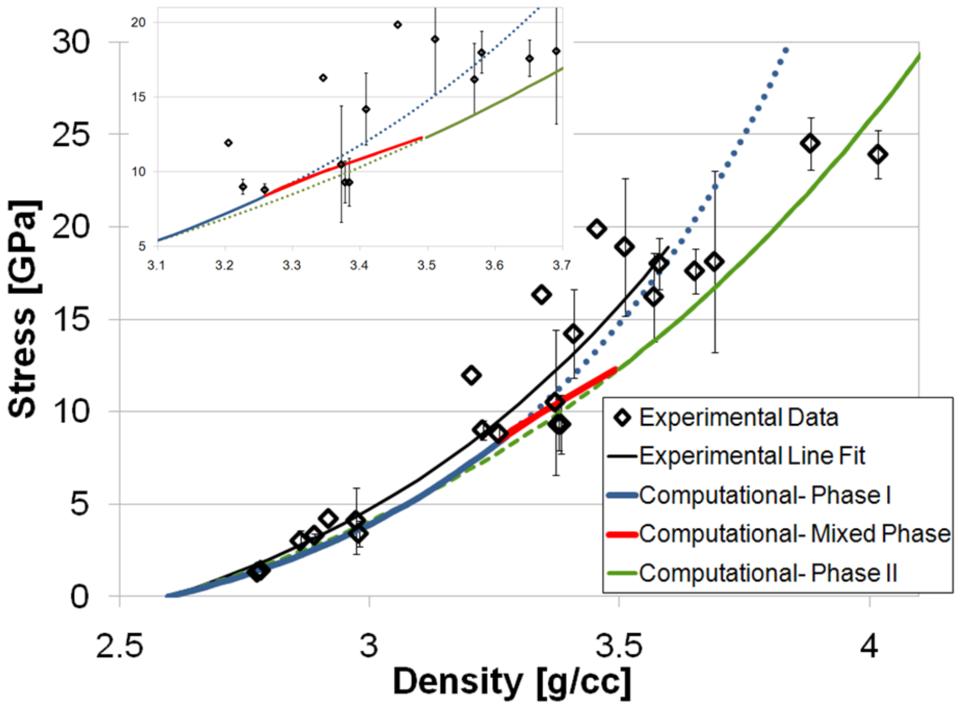

(a)

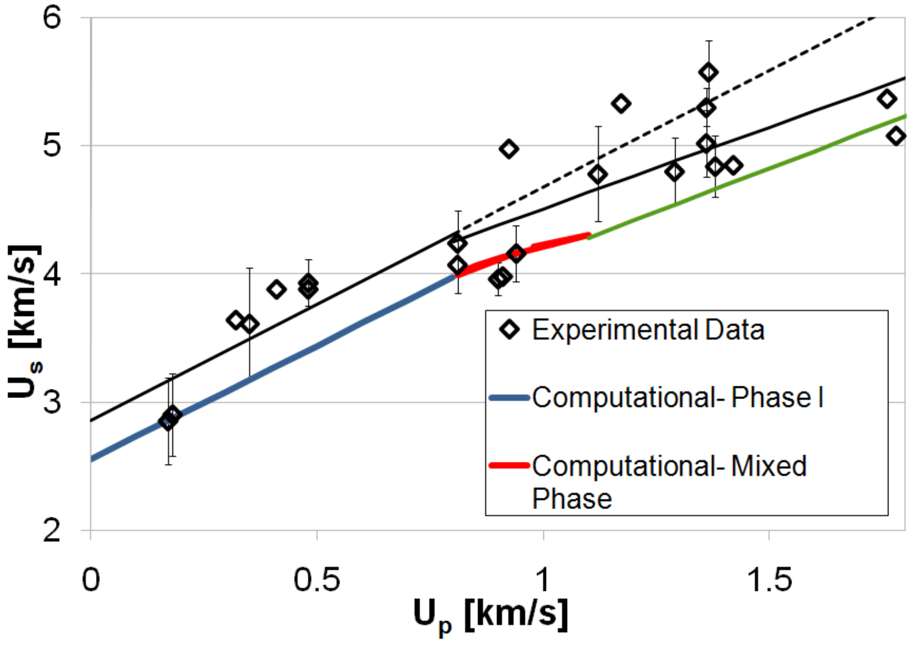

(b)

Figure 17: Bulk compaction response: experiment and simulation. Experimental data is fit to linear Us-Up and indicated by the solid black line in the figure. Dashed line is for the comparison of slopes between phase I and phase II of the epoxy

5. Investigation of the effect of multi-scale grain sizes

5.1. *Geometry*

Initially, a novel procedure was attempted to investigate the effects of grain size in mesoscale simulations with regards to hot spot formations. To reduce the computing requirement of computationally resolving nano-sized particles in a millimeter-size computational domain, a sub-grid area of investigation was selected from the mesoscale simulation. The area selected is illustrated in the upper portion of Figure 18; this area was selected due to the formation of a hot-spot. The shock appears to extrude the aluminum-binder material through the channel created by two large MnO_2 particles thereby generating very high localized shear and deformation, which results in a local hot spot.

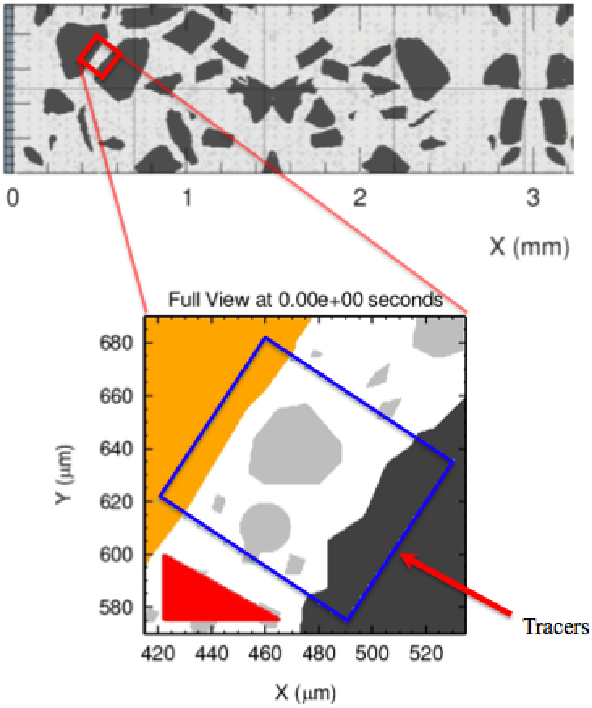

Figure 18: Area of investigation for novel attempt to simulate nano particles (nano particles are in this image, but are too small to appear on this large plot domain).

To set up the sub-grid simulations, the full domain setup discussed previously in Section 4.1 was re-computed with a box of tracers inserted in the area of interest; this was done to gather velocity data, which can then be applied as boundary conditions to the sub-grid model. Afterwards, the computational domain was cropped to the area shown above in the lower area of Figure 18. Then, the data gathered from the tracers in the full domain mesoscale simulation was used to drive a rigid plate, initially on the boundary of the tracers, through the channel in between the right and left MnO_2 particles. In addition to the driver plate, the left MnO_2 particle was also given a velocity. To compare the two domains and insure the transition from the mesoscale domain to the sub-grid domain faithfully conserves energy, the kinetic energy obtained from the tracers was compared between the full and the cut down domain. Once the energy differences were minimized, nano-sized particles were inserted into the trimmed domain. The original mass fraction of the aluminum was maintained throughout the investigation. However, due to the computing requirement to resolve nano-sized aluminum particles this process had to be abandoned. This was essentially due to the fact that at these small scales it is impossible to capture both the characteristic dimension of the particles and a representative volume.

Developing sub-grid representations in the manner described above was fraught with difficulties. The difficulties associated with resolving, what is essentially a non rectangular domain (the channel illustrated in Figure 18) with a rectangular Cartesian mesh seemed unnecessary. In addition, a small velocity gradient at the boundary was implemented which created step-wise discontinuous deformation. Finally, the morphology and roughness associated with the MnO_2 at the sub-grid scale was near the limitations of the SEM image. Thus enforcing these geometries at the sub-grid seemed unnecessary. Therefore this methodology (extracting a geometry from the mesoscale and inserting into the sub-scale) was abandoned and an alternative procedure was pursued.

Instead of using a portion of the geometry from the SEM image, the loading characteristics were applied to a representative geometry constructed from simple shapes. However, the boundary velocities extracted from the bulk mesoscale simulations were still used to establish the boundary conditions applied to a sub-grid representative volume. This resulted in a representative volume domain that could resolve nanometer particles and voids in a more computationally tractable geometry. The essential features of the flow were retained, namely extruding the binder-aluminum mixture between two large, relatively high-impedance, ceramic grains

Figure 19 presents the representative volume created in this effort. In the sub-grid domain, there are two MnO_2 grains (dark grey), one on the top and one on the bottom. In between these two MnO_2 grains are epoxy (light grey) and aluminum particles (grey) in which the size will be varied from the micron-scale down to the nano-scale. During the simulation the MnO_2 grains move towards each other at a specified initial velocity, effectively crushing and shearing the aluminum and epoxy mixture. The aluminum particles were intentionally arranged in order to simulate interesting grain scale dynamics observed from previous mesoscale simulations [31, 32]. Specifically these include the formation of dynamic stress bridges, which is facilitated by grains loosely arranged in the direction of the shock. This effect will be enhanced given that the grain arrangement is percolated through the domain. The novel idea pursued here is using boundary conditions extracted from the bulk mesoscale simulations in order to drive a subscale simulation exploring the role of nano-particles and strain hardening constitutive relations.

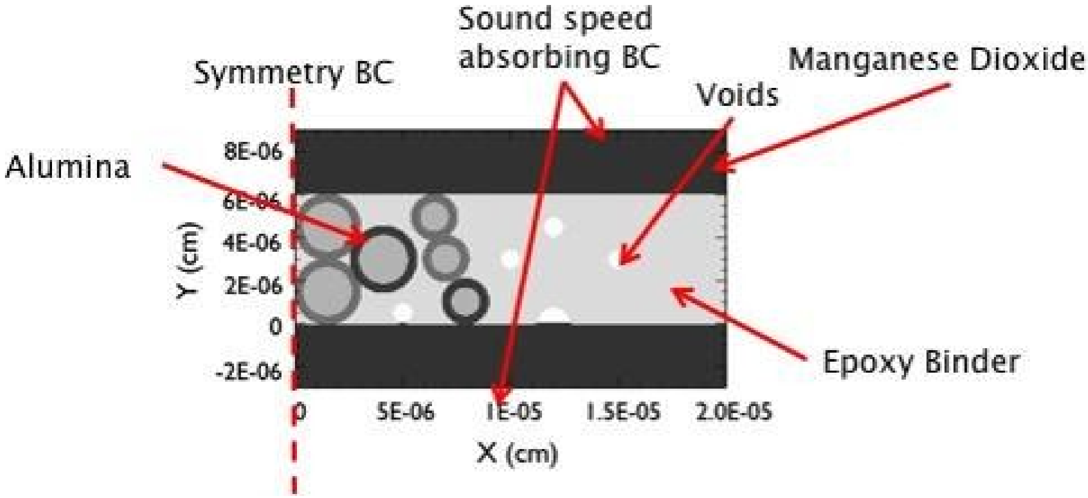

Figure 19: Computational domain utilized in the multiscale investigation

The scale of the computational domain, as presented in Figure 19, was varied in order to investigate a large range of particle sizes within the test matrix and the effect of varying the length scale while enforcing a strain-rate constitutive model. In addition, the thickness of the alumina (Al_2O_3) coating was varied, which effectively changes the overall density and yield strength of the aluminum particles. The thickness of the coating was varied between 0 and 3 nm [33]. Removing the alumina coating at the nano scale was done to more faithfully compare the effect of particle size variations from millimeter to nanometer scales without the complications associated with simultaneously changing the density and bulk mixture yield strength.

5.2. *Numeric Setup*

The MnO_2 particles on the top and bottom of the domain both compressed the epoxy and aluminum particles at speeds of -450 m/s and 450m/s respectively; these velocities were extracted and representative of the average particle velocities observed in the MnO_2 during the sub-grid compaction event [31]. The top and bottom boundary conditions are such that the sound speed is transmitted (semi-infinite solid), while the MnO_2 simultaneously continues to flow into the computational domain from the top and bottom as the simulation progresses. This saved the computational expense associated resolving large volumes of MnO_2. Symmetry was imposed along the x=0 axis (the domain is mirrored about x=0). The right boundary imposed zero pressure and mass removal in the ghost cells; no mass can enter along the boundary, but mass can exit. Due to the symmetry of the domain and the boundary conditions, a large shear gradient was established in the epoxy/aluminum mixture as the mixture is extruded to the right.

5.3. *Material Properties*

The material properties used in this process were all the same as from Section 4.3. In addition, aluminum oxide was used as a coating around the pure aluminum alloy. A Johnson-Cook model and a Mie-Gruneisen equation of state were used to model the alumina. Because these are mesoscale computations, various nanoscale particle effects, such as phonon scattering at the interfaces, are not accounted for. The material properties can be seen in Table 4. The fracture strength was turned on for the multiscale investigation. Previously the fracture strength was effectively turned off by giving all materials a fracture strength that was unattainable. The reason both the Johnson-Cook and Johnson-Holmquist II models were chosen in Section 4.3 was to incorporate strain-rate dependent behavior in the simulations. If this was not done and only elastic-perfectly plastic models were used for each material, the results would scale exactly with the domain size.

Table 4: Equation of State and Constitutive Material Parameters II

Parameter	**MnO2**† [22,23,24]	**Al** [25’26]	**Epoxy**†† Phase I [22,27,28]	**Epoxy** Transition Phase [22,27,28]	**Epoxy** Phase II [22,27,28]	**Al2O3** [22,34]
Density, ρ [*g/cm3*]	4.55	2.703	1.19	1.19	1.19	3.69
Zero stress shock speed, C_0 [*km/s*]	3.632	5.288	2.67	7.88	2.88	0.987
Hugoniot slope, s	1.52	1.3756	1.55	0.01	1.35	8.71
Grüneisen coefficient, G=$V(\partial P/\partial E)_V$	1.25	2.14	2.18	2.18	2.18	2.14
Specific heat, C_V [*J/(g-K)*]	0.67	0.885	2.1	2.1	2.1	0.885
Bulk Dynamic yield strength, Y [*GPa*]	7.5	0.29	0.069	0.069	0.069	15.4
Poisson's ratio, ν	0.28	0.32	0.36	0.36	0.36	0.21
Bulk Modulus, K [*GPa*]	34.4	N/A	8.48	73.9	9.87	N/A
Fracture strength, σ_s [*GPa*]	N/A	0.31	0.013	0.013	0.013	0.31

5.4. Results

Material plots were generated to explore the grain interactions within the domain as well as identify regions that generate the highest temperature. Figure 20 presents an example where the hotter areas are at the edges where the three large aluminum particles are in contact and at the shear bands in the MnO_2.

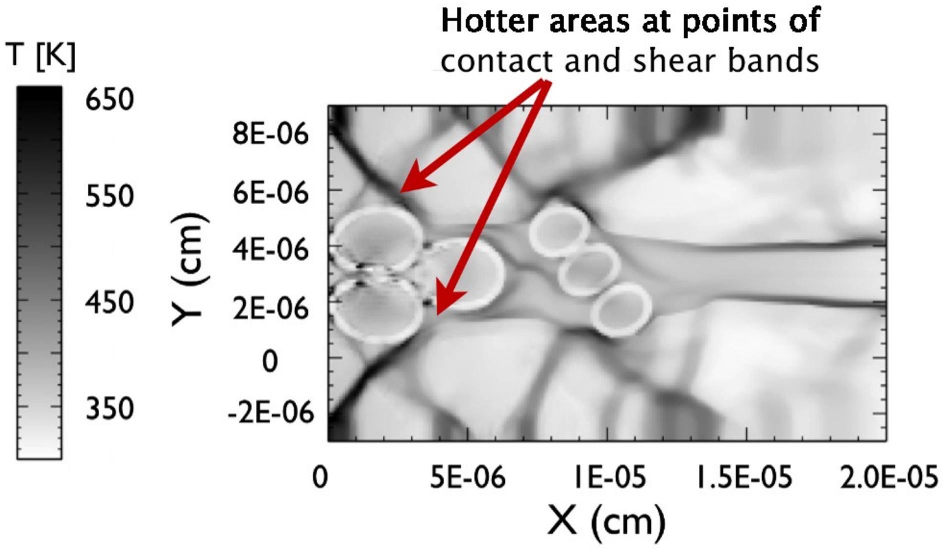

Figure 20: Temperature contour of aluminum particles with a 3nm alumina coating at 110ps (t/t_0=0.44).

In addition, a plot was made with the maximum temperature within the entire computational domain at each time step; see Figure 21. This method was chosen for simplicity to check if there are any potential temperature changes in the hot regions as the aluminum particle size is varied. The time has been normalized by the simulation time in order to compare temperature profiles across a wide range of scales. As the particle size was varied from milli-sized to nano-sized, the maximum temperatures reached are slightly increased due to the strain hardening associated with higher local strain rates. When the alumina coating was varied from 1 to 3 nm, the maximum temperature varied to some extent, though no pattern of behavior can be conclusively detected.

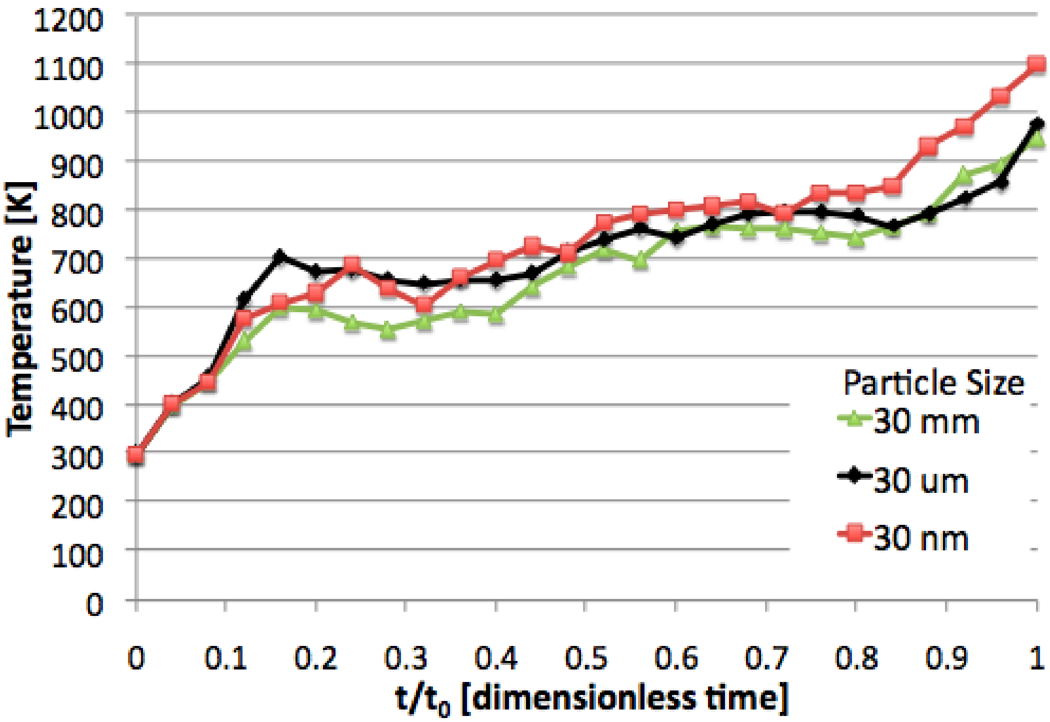

Figure 21a: Maximum temperature achieved in the domain as a function of dimensionless time step. (a) Variations in particle size.

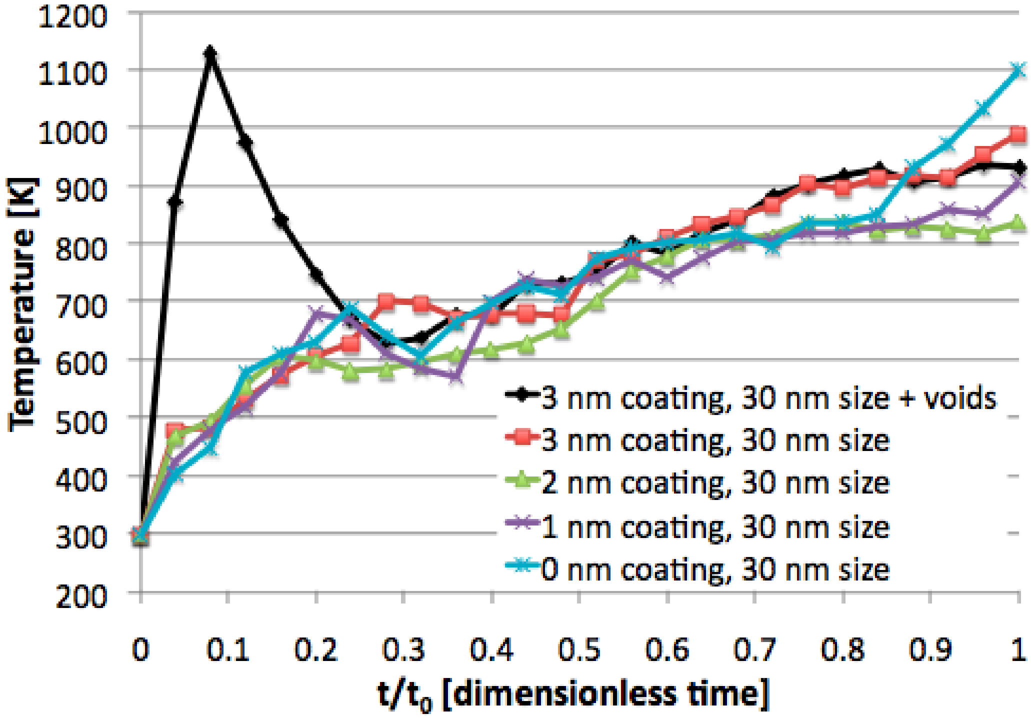

Figure 21b: Maximum temperature achieved in the domain as a function of dimensionless time step. (b) Variations in coating/adding voids

Lastly, a simulation was performed in which voids within the epoxy binder were inserted into the domain to compare the effect of void collapse relative to strain hardening. The geometry with the voids can be seen in Figure 22. It is well known that voids cause hot spots to occur and can cause ignition in reactive materials [35]. The reason for adding them in this case was to compare the effect on the temperature around the voids with the effect of changing the particle size and alumina coating. As shown in Figure 21b, the voids can increase the local temperature by nearly 600 K as opposed to not having a void. This increase in temperature is sustained for nearly 30 ps, after which, the temperature profile approaches the simulations without initial voids.

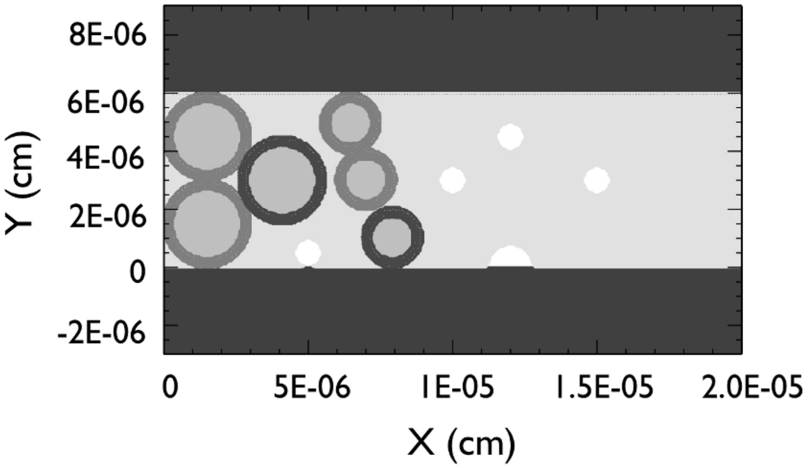

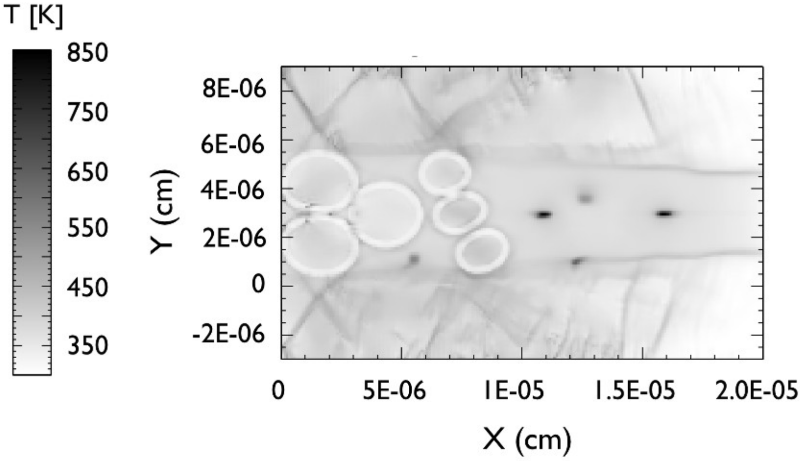

Figure 22: (Top) Geometry setup at 0.0 s with a 3 nm thick oxide layer and voids in the epoxy. (Bottom) Temperature contour at 40.1 ps (t/t0=0.16); note hot spots corresponding to initial voids inserted in the epoxy.

5.4.1. Conduction

Conduction calculations were also performed for the case of a 30 nm aluminum grain in the same way as described for a 20 μm grain in Section 4.4.2. Assuming a same shock speed of 2.9 km/s, the time under strain was found to be 5.17 ps. Using this value, the distance of heat conducted was found to be 36.67 nm. Notice now that conduction is now significant in the nanoscale case. Again, this will be a possible area of future investigation where the simulations include model the effects of conduction.

6. Conclusions

The main goal of this thesis was to investigate the dynamic behavior of the Al-MnO_2-Epoxy mixture using experimental and computational data. In the first part, CTH was used to model the shock compaction of the mixture at particle velocities ranging from 180 m/s to 2770 m/s. The Johnson Cook and Johnson Holmquist strength models were used for the aluminum and manganese dioxide respectively; these models are strain rate dependent and will capture the strain hardening or softening the materials undertake when they are compressed. For the epoxy, an elastic-perfectly plastic strength model was used. The Mie-Gruneisen equation of state model was used for the aluminum and epoxy, while the manganese dioxide equation of state was built in to the Johnson Holmquist model. The computational results were then compared with experimental data gathered at NSWC-IH and LANL. The two data sets were shown to be in agreement with one another.

In the second part, a representative volume was created to perform a computational multiscale investigation on the mixture. The aluminum grain size was varied from 30 mm to 30 nm. Also, the aluminum oxide coating was varied, effectively changing the overall strength of the grains. The results of these simulations were not as conclusive as expected; only a slight trend could be seen as the grain sizes were varied and no pattern was apparent when the aluminum oxide coating was varied.

7. References

[1] McGlaum, J.M., Thompson, S.L., and Elrick, M.G. Int. J. Impact Eng. 10, (1990), 351-360.

[2] Borg, J.P., and Vogler, T.J., Int. J. Solids Struct. 45, (2008), 1676–1696

[3] Baer, MR, Thermochimica Acta. 384, (2002), 351-367

[4] Benson, D.J. and Conley P., Modelling Simul. Mater. Sci. Eng. 7, (1999), 333-354

[5] Salas, Manuel D., "The Curious Events Leading to the Theory of Shock Waves." Proceedings of the 17th Shock Interaction Symposium, September 4-8 2006.

[6] Hayes, D.B., Introduction to stress wave phenomena. 1973, Lecture Notes.

[7] Millet, J.C.F., Deas, D, Bourne, N.K., Montgomery, S.T. "The deviatoric response of an alumina filled epoxy composite during shock loading." J. Appl. Phys. **102**, 063518 (2007)

[8] Ferranti, L., Jordan, J.L., Dick, R.D., Thadhani, N.N. " Shock Hugoniot behavior of particle reinforced polymer composites." In *Shock Compression of Condensed Matter- 2007*, edited by M.D. Furnish, American Institute of Physics, 2007 p. 123-126

[9] Benson, David J, "Numerical Methods for Shocks in Solids." *Shock Wave Science and Technology Reference Library.* Springer Berlin Heidelberg. 2007, Pp. 275-320

[10] Eakins, D. and Thadhani, N.N., J. Appl. Phys. **101**, 043508 (2007)

[11] Baer, M.R., Hall, C.A., Gustavsen, R.L., J. Appl. Phys. **101**, 034906 (2007)

[12] Baer, Mel R., "Mesoscale Modeling of Shocks in Heterogeneous Reactive Materials." *Shock Wave Science and Technology Reference Library.* Springer Berlin Heidelberg. 2007, Pp. 321-356

[13] Jordan, JL., Dattelbaum, DM, Sutherland, G, Richards, WD, . Sheffield, SA, and Dick J. of App. Phys. (under preparation)

[14] GNU Image Manipulation Program

[15] Raster to Vector Conversion Toolkit, v. 2.97.62, Algolab Inc.

[16] AutoCAD 2008. Autodesk. San Rafael, CA. 2008

[17] MATLAB R2008a. The Math Works. Natick, MA. 2008

[18] Zerelli, F. J., and Armstrong, R. W., J. Appl. Phys, 61, 1816–1825 (1987).

[19] Meyers, Marc A., *Dynamic Behavior of Materials*. John Wiley and Sons, Inc., 1994

[20] Johnson and Holmquist, High-Pressure Science and Technology, 309, AIP Press, (1994) 981-4

[21] Carter, WJ and Marsh, SP. "Hugoniot Equation of State of Polymers." LANL. LA-13006-MS. 1995

[22] Marsh, S.P. LASL Shock Hugoniot Data (1980)

[23] Wang, Y, Zhang, J and Zhao, Y, *Nano Letters* 7, (2007), 3196-3199

[24] Swamy, V., *Phys. Rev. B.* 71, 184302 (2005)

[25] Steinberg, D.J., LLNL, UCRL-MA-106439, 1991

[26] Moshe, E., et. al., J. Appl. Phys. 83, 4004, 1998

[27] Austin, R, McDowell, D, and Benson, D. Modelling Simul. Mater. Sci. Eng. 14 (2006) 537-561

[28] Richard C., Ting, R.Y., Audoly, C., "Development of 1-3 PZT-Polymer Composite for low frequency acoustical applications." Proceedings of the Ninth IEEE International Symposium on Applications of Ferroelectrics, 1994.ISAF, August 7-10 1994. 291-294

[29] Kerley, GI "CTH Equation of state package: porosity and reactive burn models" Sandia National Laboratories report SAND92-0553, 1992

[30] Jensen, J.E., Tuttle, W.A., et. al. BNL 10200-R 1980

[31] Fraser, A., Borg, J.P., Jordan J.L., Sutherland, G. “Exploring the micro-mechanical behavior of Al-MnO_2-Epoxy under shock loading while incorporating the epoxy phase transition”, SEM Annual Conference & Exposition on Experimental & Applied Mechanics, Albuquerque, NM, 2009

[32] Borg, JP and Vogler, TJ “Aspects of simulating the dynamic compaction of a granular ceramic.” Modelling and Simulation in Materials Science and Engineering. 17, 045003, (2009) pg 1-22

[33] Risha, G.A. et al. “Combustion of nano-aluminum and liquid water”, Proceedings of the Combustion Institution 31 (2007) 2029-2036

[34] Alexander, William, Shackelford, James *CRC Materials Science and Engineering Handbook.* CRC Press. 3rd Edition, 2001.

[35] Bowden, F.P. and Yoffe, Y.D. *Initiation and Growth of Explosions in Liquids and Solids*. Cambridge Univ. Press, New York, 1951

8. Appendices

8.1. Settings for image importation process

Algolab Recognition Parameters:

- Outlines
- 4 min pixel length
- Lines
- Curves-10 iteration number-represented by lines
- 5 angle sensitivity

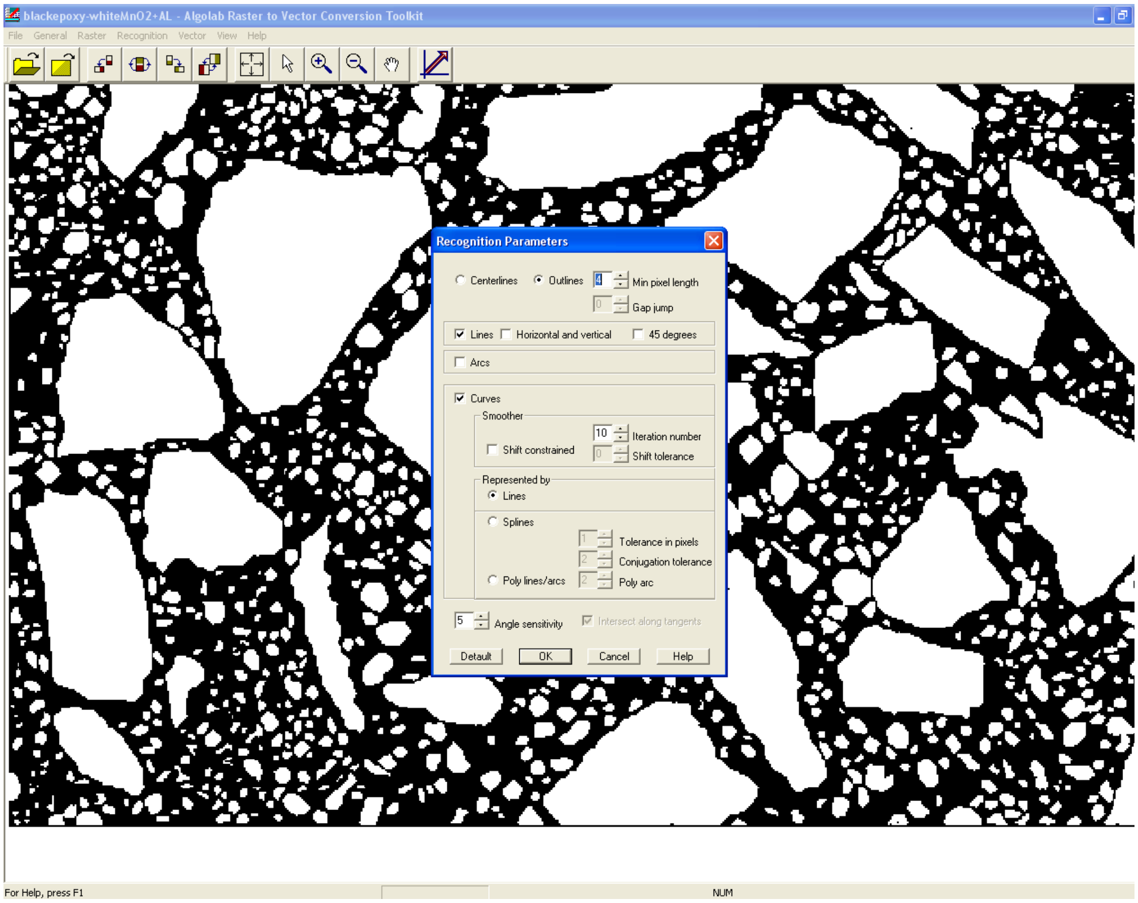

Recognition Parameters

○ Centerlines ● Outlines 4 Min pixel length

0 Gap jump

☑ Lines ☐ Horizontal and vertical ☐ 45 degrees

☐ Arcs

☑ Curves

Smoother

10 Iteration number

☐ Shift constrained 0 Shift tolerance

Represented by

● Lines

○ Splines

1 Tolerance in pixels

2 Conjugation tolerance

○ Poly lines/arcs 2 Poly arc

5 Angle sensitivity ☑ Intersect along tangents

8.2. Calculations for conduction

<u>For 20 μm grain:</u>

$d = 2\sqrt{\alpha t}$ Where *d* is the distance heat is conducted, α is the thermal diffusivity, and *t* is the time under strain

$\alpha = 0.65 cm^2/s$ for aluminum [2]

$t = \frac{10x10^{-6} m}{2.9x10^{3} m/s}$ →Using the slowest shock speed leading to the largest conduction value

$t = 3.448x10^{-9} s$

$\boxed{d = 0.947 \mu m}$

<u>For 30 nm grain:</u>

$t = \frac{15x10^{-}\ m}{2.9x10\ m/s}$

$t = \quad 0^{-}\ s$

$d = \quad 0^{-}\ cm$

$\boxed{d = \quad}$

---

[2] Jensen, J.E., Tuttle, W.A., et. al. BNL 10200-R 1980

8.3. Full domain material plots

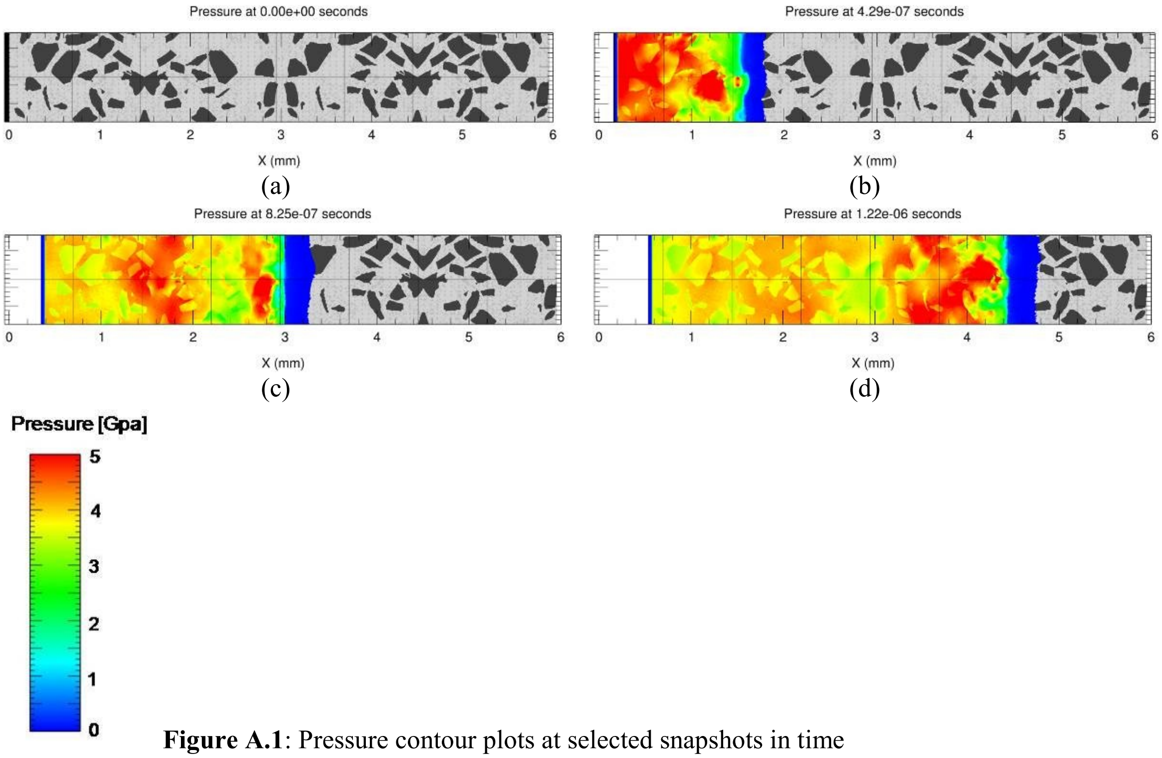

(a) (b)

(c) (d)

Figure A.1: Pressure contour plots at selected snapshots in time

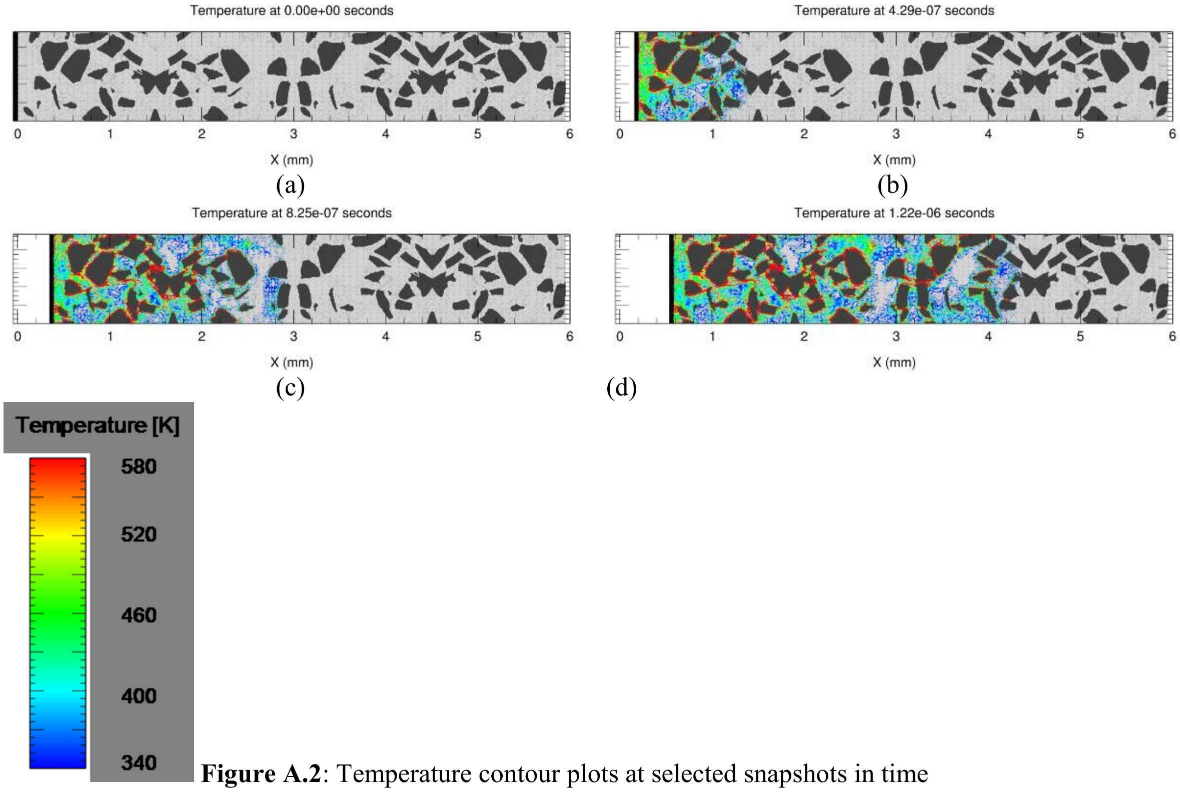

(a) (b)

(c) (d)

Figure A.2: Temperature contour plots at selected snapshots in time

8.4. Representative domain material plots

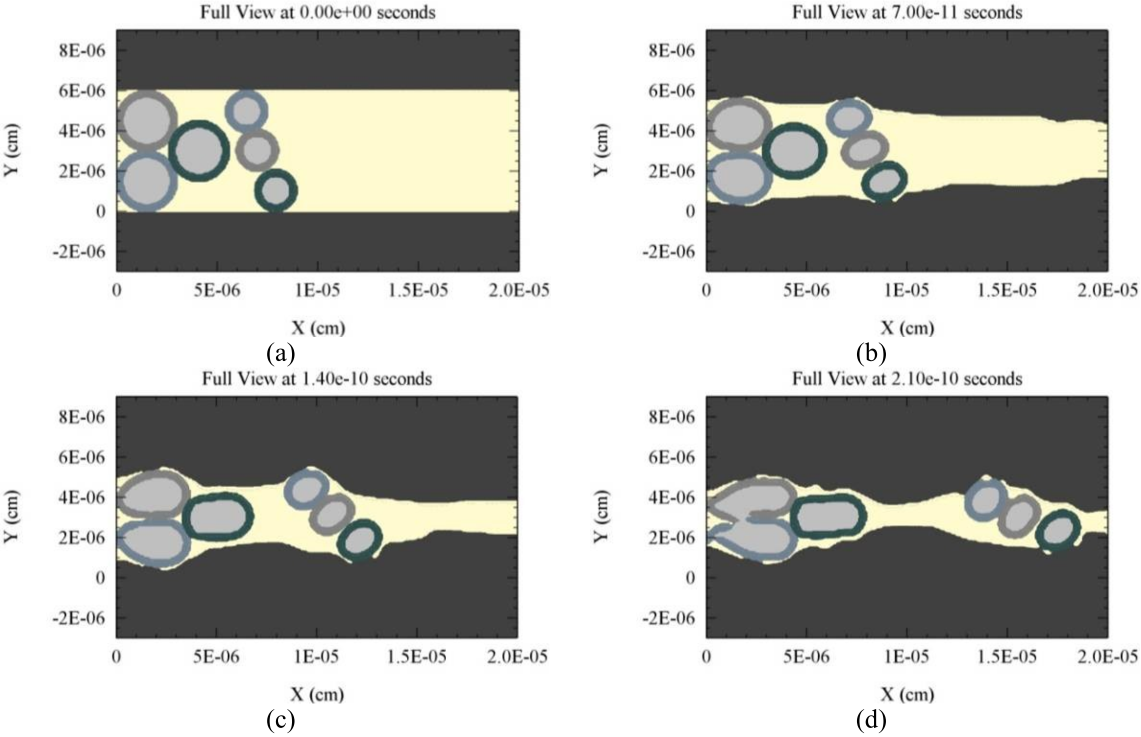

(a) (b) (c) (d)

Figure A.3: Material plots at selected snapshots in time

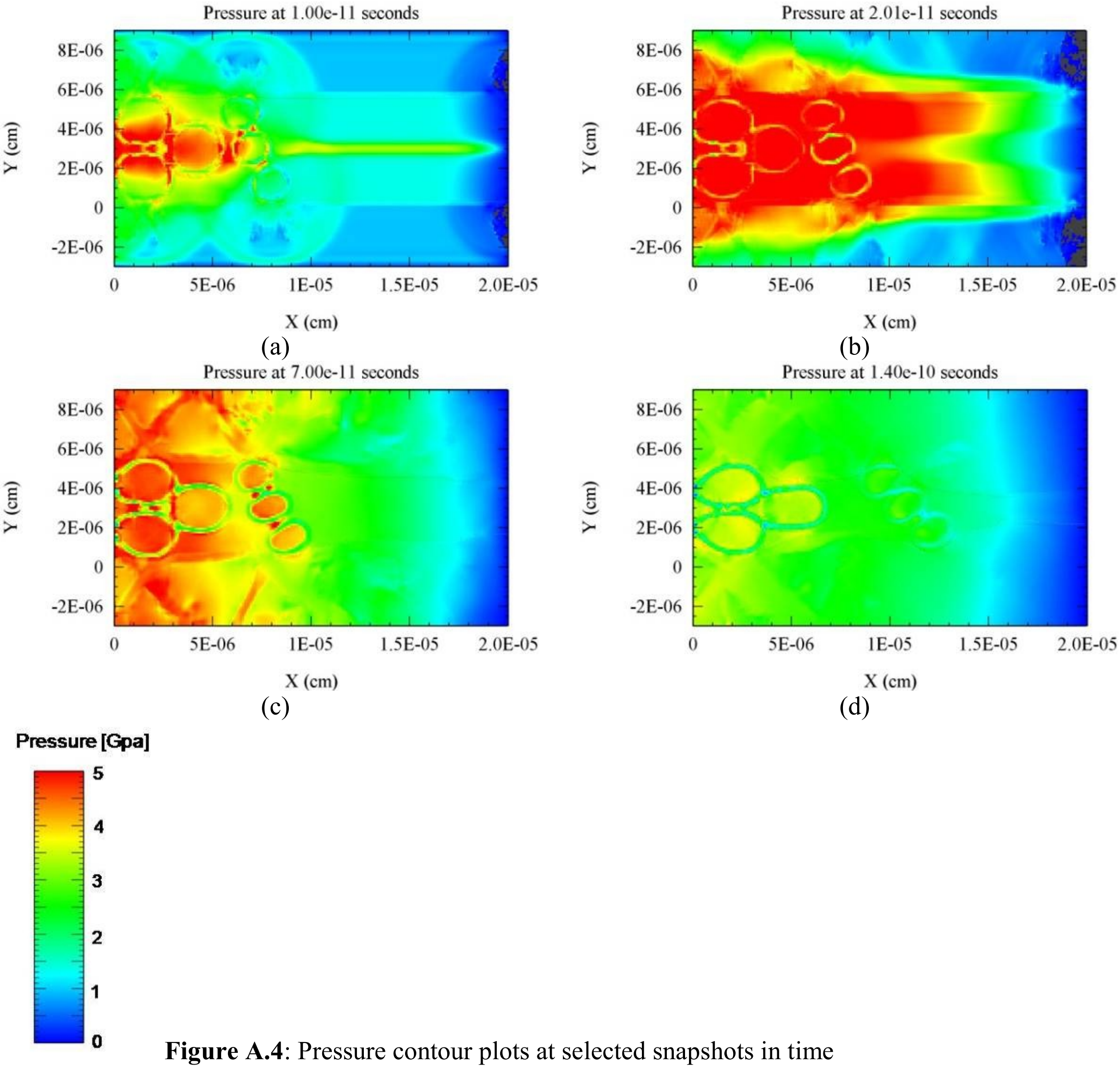

(a) (b) (c) (d)

Figure A.4: Pressure contour plots at selected snapshots in time

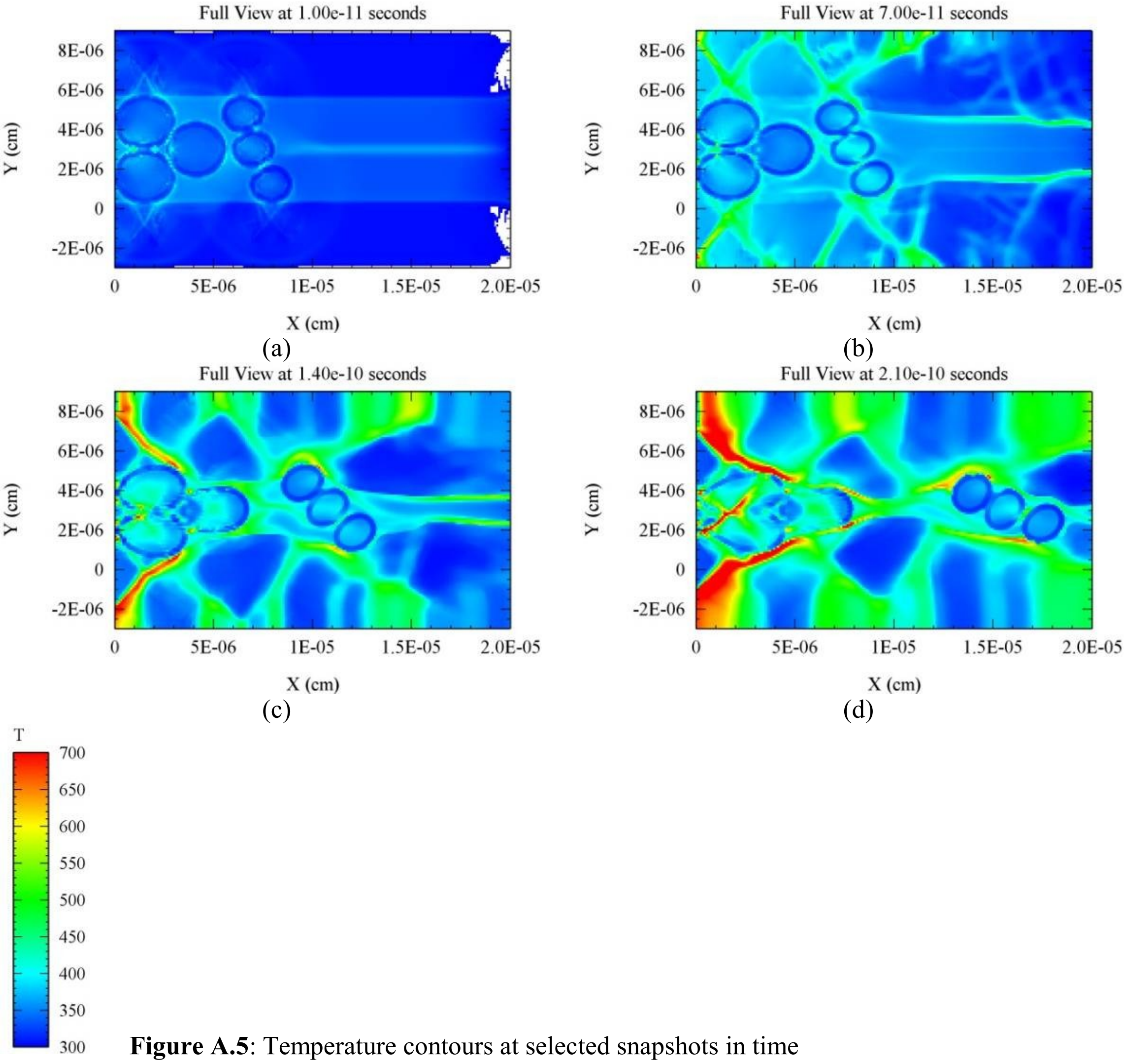

(a) (b) (c) (d)

Figure A.5: Temperature contours at selected snapshots in time